International Journal of Mechanical Sciences 228 (2022) 107507

Contents lists available at ScienceDirect

International Journal of Mechanical Sciences

journal homepage: www.elsevier.com/locate/ijmecsci

Numerical study and topology optimization of vibration isolation support structures

Haojiang Zhao [a], Yang Feng [a,b,*], Wei Li [a], Chuang Xue [a]

[a] Changchun Institute of Optics, Fine Mechanics and Physics, Chinese Academy of Science, Changchun 130033, China
[b] University of Chinese Academy of Sciences, Beijing 100049, China

ARTICLE INFO

Keywords:
Topology optimization
Phononic crystals
Coupling design
Genetic algorithm
Vibration isolation

ABSTRACT

Lightweight design and harmful vibration isolation of supporting structures are the most common design contents in practical engineering, but they are often difficult to be considered together. Phononic crystals have the characteristics of elastic wave bandgaps, which can effectively isolate the vibration within the bandgap frequency range. The integrated coupling design of vibration isolation and structure support by topology optimization is studied in order to make the obtained macro structure with periodic characteristics have both high support structure stiffness and lower frequency vibration isolation bandgaps. Taking a two-dimensional cantilever beam with multiple periodic substructures in the length direction for example, the finite element method and an improved multi-objective genetic algorithm are used to realize the topology iterative change of the substructure mesh, the solution of the substructure band structure and the natural frequency of the cantilever beam. Maze algorithm is used to avoid invalid operation in optimization process and the mesh generation strategy combining coarse mesh and fine mesh is taken to improve the operation efficiency. Two optimization objective functions reflecting the overall support stiffness and relative bandgap width of the cantilever beam are set. The topology design of the substructure with transverse symmetry constraints and bisymmetric constraints are carried out, respectively. The topology optimized structures with bandgaps of different mechanisms are obtained from the Pareto front of the numerical results.

1. Introduction

In various engineering fields related to mechanical design, the use of important equipment mostly has the requirements of both lightweight design of support structure and harmful vibration control. The support structure is the intermediate link between the equipment and the installation platform. On the premise of meeting the dynamic and static mechanical characteristic indexes such as support stiffness and natural frequency, the reasonable lightweight design of the support structure can significantly reduce the manufacturing cost and use cost caused by weight. The suppression of harmful structural vibration is another important issue to be considered when supporting the equipment. Good vibration isolation measures can effectively improve the safety, reliability and performance stability of the equipment. At present, the vibration isolation performance is not considered in the lightweight design of most support structures, and only taking the dynamic or static stiffness as the optimization object [1–3].The disadvantage of this traditional lightweight design idea is that the designed support structures has no vibration isolation effect or the vibration isolation effect is very weak. The independently designed active and passive vibration isolators or vibration isolation structures add additional weight after they are installed on the main support structure [4]. Therefore, it is of great practical value to study the lightweight design method of structure taking into account the functions of vibration isolation and support.

The concept of phononic crystals (PnCs) [5–9] provides a new solution for vibration suppression. PnCs are a kind of artificial periodic material with elastic wave band gap, and the vibration form in the band gap frequency range cannot pass through, so it can be used in the field of vibration isolation [10–15]. Compared with the traditional active and passive vibration isolation methods, PnCs based vibration isolation has the advantages of light weight [16,17], wide vibration isolation frequency range [18–20] and high reliability. It has a wide application prospect in the field of engineering vibration isolation. A large number of scholars have carried out the research of PnCs vibration isolation. In order to obtain the vibration band gap in a wider and lower frequency

* Corresponding author at: Changchun Institute of Optics, Fine Mechanics and Physics, Chinese Academy of Science, Changchun 130033, China.
E-mail address: fengyang20@mails.ucas.ac.cn (Y. Feng).

https://doi.org/10.1016/j.ijmecsci.2022.107507
Received 29 December 2021; Received in revised form 30 June 2022; Accepted 30 June 2022
Available online 1 July 2022
0020-7403/© 2022 Elsevier Ltd. All rights reserved.

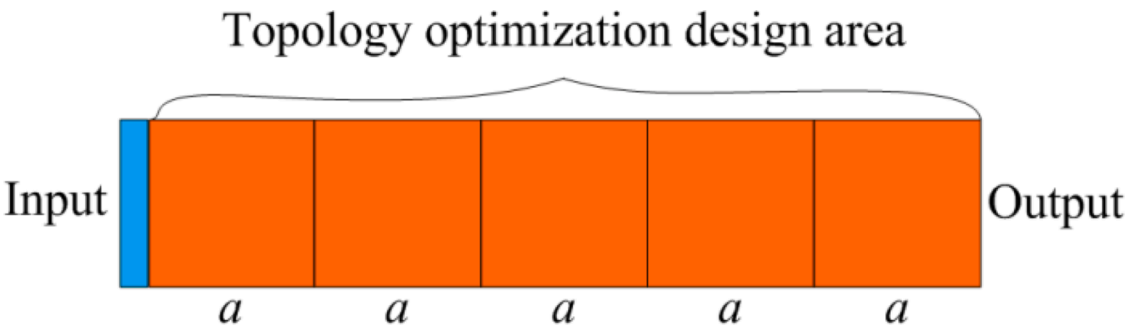

Fig. 1. (color online) The cantilever beam and its substructures in the example.

range, the design of new PnCs [21–30], the enhancement effect of viscoelastic materials on the vibration attenuation in the band gap [31, 32] and the tunability of band gaps [33–35] have attracted much attention. In addition, it is also an effective means to obtain PnCs with better vibration isolation performance through topology optimization design [36,37]. There are many algorithms that can be used to optimize the topology of PnCs, such as the solid isotropic material with penalization (SIMP) method [38], the bi-directional evolutionary structural optimization (BESO) [39–43], the gradient-based optimization methods [44,45], different kinds of genetic algorithms (GA) [46–60] and some other methods [61–63]. The 0∼1 coding mechanism for design variables of GA [64] is perfectly matched with the material mesh representation method of '0 removal while 1 retention' in the topology optimization process, and GA also has lower requirements for the mathematical description of the optimization problem. Hedayatrasa et al. [65] used multi-objective GA and finite element method (FEM) to optimize the topology of one-dimensional periodic bimaterial PnC, and realized the maximum relative band gap width under low-order Lamb waves. By using a "coarse to fine" two-stage GA as the inverse search scheme, Dong et al. [66] performed both the unconstrained and constrained optimal design of the unit cell topology of the two-dimensional square-latticed solid PnCs, to maximize the relative widths of the band gaps.

The band gap characteristics of PnCs with different component fractions (single phase [45], two phases [49–52,56], three phases [53, 60] and more phases [67,68]) were studied. Generally speaking, increasing the number of materials in PnCs can produce richer band gap characteristics, but the manufacturing difficulty and uncertainty will also increase [62,69,70]. Zhang et al. [70] proposed a robust topology optimization method of PnC microstructures against random diffuse regions between material phases. Numerical examples showed that the proposed method provided meaningful optimal designs of microstructures of the unit cell in achieving a robust band gap. The symmetry of the material layout in the cell of PnCs has been proved to have an important impact on the band gaps distribution [53,56,58,71]. Results showed that the reduction of the symmetry of the unit cell can be helpful to obtain the wider band gaps. In order to obtain the band gaps in a lower frequency range, soft materials (such as rubber) were used as the continuous phases in PnCs [34,72–74], and the connection stiffness between and within the unit cells were weakened [44,75–78]. Aiming to broaden and manipulate the low frequency band gaps, an innovative structure with filling materials in a square lattice of silicone rubber was proposed, where the spatial distribution of the materials had been optimized using an improved GA [73]. Zhang and Han [74] designed a hybrid PnC consisting of rubber slab with periodic holes and Pb stubs to obtain wider band gaps in low frequency range. The wider band gap can be attributed to the interaction of local resonance and Bragg scattering. Yang et al. [77] proposed a topology optimization method directly using the effective mass density concept to maximize the first bandgaps of two-dimensional solid Locally Resonant Acoustic Metamaterials (LRAMs). The coating layer interfacing the core and the matrix of the ternary LRAM was chosen as the design region because it significantly influences the bandgaps. The materials of the matrix, coating, and core are epoxy, rubber and lead, respectively. Yuksel and Yilmaz [78] designed a two-dimensional solid structure with embedded inertial amplification mechanisms that showed an ultrawide band gap at low frequencies. In the compliant inertial amplification mechanism with length as 157 mm and width as 85.4 mm, the flexure hinge thicknesses were only set as 0.3 mm. Although the obtained periodic structures by these measures have lower and wider band gaps, their structural stiffness have been seriously weakened, which is not enough to support other loads, and even does not have the stiffness to support themselves. Such kind of periodic vibration isolation structures are difficult to apply in practical engineering.

Only a few literatures have paid attention to the stiffness and strength of PnCs structures [67,79–84]. Zhu et al. [67] proposed a chiral lattice-based elastic metamaterial beam with multiple embedded local resonators to achieve broadband vibration suppression without sacrificing its load bearing capacity. These local resonators, made of rubber coated steel cylinders as well as tungsten cylinders, are filled in the node circles of the aluminum chiral honeycomb beam. Chen et al. [79] applied the BESO algorithm for the optimal design of 2D viscoelastic PnCs. The resulting viscoelastic PnCs had the maximum attenuation property of elastic waves at the specified frequencies, and meanwhile possessed a prescribed stiffness by the bulk modulus constraints. Chen and Wang [80] constructed a class of honeycombs with hierarchically architected structure by replacing the cell wall of regular honeycomb with hexagonal, kagome and triangular lattice, respectively. The introduction of structural hierarchy produced broad and multiple phononic band gaps and endowed the honeycomb with enhanced stiffness. Andreassen and Jensen [81] optimized the distributions of a stiff low loss and a soft lossy material in order to maximize the attenuation. Dong et al. [82] studied the topology optimization of 2D phoxonic crystals (PxCs) with simultaneously maximal and complete photonic and phononic bandgaps. The optimized structures were composed of solid lumps with narrow connections, and their Pareto-optimal solution set can keep a balance between photonic and phononic bandgap widths. Refs. [81, 82] both considered the issue of stiffness constraint by requiring the homogenized elastic modulus to be greater than the specified threshold. Porous phononic crystal plates were optimized by non-dominated sorting genetic algorithm(NSGA-II) to obtain the widest bandgaps and maximized stiffness [83,84]. The objective function reflecting the maximum stiffness was defined as the minimum relative strain energy compliance of the unit cell. In the above literature, although obtained PnC structure has a certain stiffness by selecting rigid materials, imposing stiffness constraints or taking the stiffness of single cell as one of the most optimization objectives, the macro stiffness requirements of finite PnCs as supporting structure have not been integrated into the topology design of its unit cell.

Based on the above analysis, taking a single material two-dimensional cantilever beam as an example, this paper attempts to integrate the PnC band gap optimization with the lightweight design of the support structure by using an improved GA, so as to obtain a

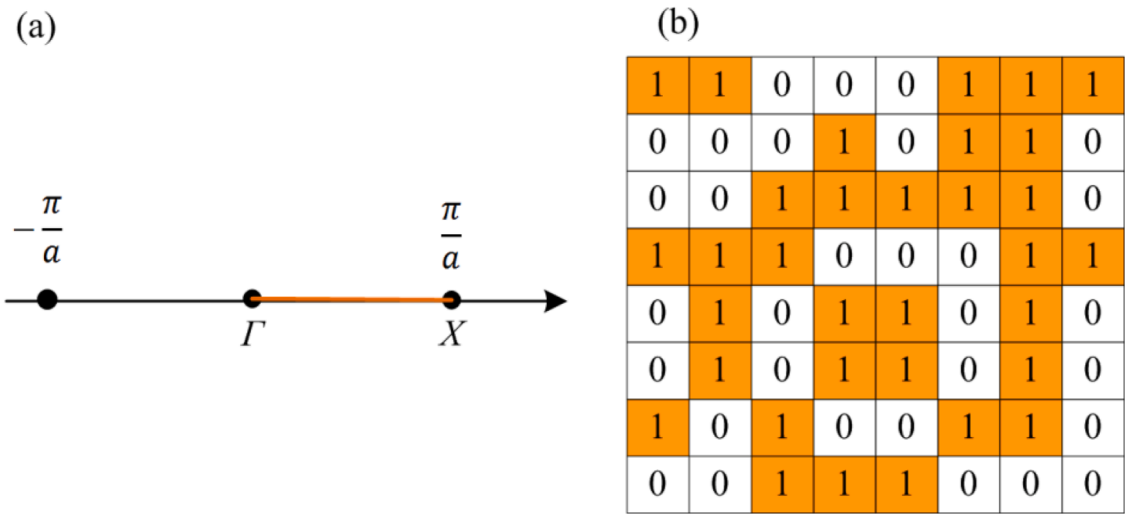

Fig. 2. (color online) (a) The Brillouin zone of one-dimensional periodic structure, here, a is the lattice constant, X and Γ are points with high symmetry of the reciprocal lattice space; (b) one example of 0~1 grid matrix of substructure, where the virtual mesh (the area where the material is removed) is represented by $x = 0$, and the real mesh (the area where the material is retained) is represented by $x = 1$.

lightweight cantilever beam with periodic microstructure. So that the beam can meet a certain support stiffness, at the same time, it has vibration isolation characteristics in a lower frequency range. Through this new idea, it is expected to promote the practical process of PnCs vibration isolation and combine the vibration isolator and lightweight support structure into one.

2. Problem description

Taking the single material two-dimensional cantilever beam structure shown in Fig. 1 as an example, the lightweight topology optimization design of the cantilever is carried out to make the cantilever have a higher fundamental frequency and lower and wider vibration band gap. In order to introduce the band gap characteristic of periodic structure to realize vibration isolation, the cantilever beam is divided into several substructures with equal length along the length direction. These substructures have one-dimensional periodic repeatability in the length direction of the beam. Taking any substructure as the topology optimization region, and copying the topology of the substructure to other substructures, a cantilever overall support structure with periodic topology characteristics can be formed. The number of substructures divided by a finite length cantilever beam will affect the topology optimization results, but it is not discussed in this paper. It is assumed that in the calculation example, the total length of the cantilever beam is $5a$ and the width is a, and the length of the substructure is consistent with the width of the cantilever beam. The transverse or longitudinal harmonic acceleration excitation input is applied on the left end of the model, and the acceleration response output is received and recorded on the right end.

The substructure is divided into meshes of n rows and m columns, the design variable x can only take values of 0 and 1. The virtual mesh (the area where the material is removed) is represented by $x = 0$, and the real mesh (the area where the material is retained) is represented by $x = 1$, so as to obtain the 0~1 mesh matrix of the substructure. Therefore, the integrated topology optimization model of vibration isolation and support of cantilever beam in this example can be expressed as:

$$\text{Find}: X_{\text{cell}} = \begin{bmatrix} x_{11} & x_{12} & \cdots & x_{1n} \\ x_{21} & x_{22} & \cdots & x_{2n} \\ \vdots & \vdots & \vdots & \vdots \\ x_{m1} & x_{m2} & \cdots & x_{mn} \end{bmatrix}, \; x_{ij} \in [0,1] (i = 1, 2, \cdots, n; j = 1, 2 \cdots m)$$

$$\text{Minimize}: \begin{cases} T_1 = \dfrac{f_{gc1}}{f_{mod1}} \\ T_2 = \dfrac{f_{gc1}}{\mathrm{w}_{\mathrm{gc1}}} \end{cases} \tag{1}$$

Here, X_{cell} is the 0~1 design variable matrix which have a size of $n \times m$; f_{gc1} is the central frequency of the first vibration band gap of the substructure; f_{mod1} is the fundamental frequency of cantilever beam; w_{gc1} is the band gap width; T_1 *and* T_2 are the objective functions. In general, for the periodic structure composed of the single material, the low-frequency band gap is contradictory to the overall high stiffness of the structure. Therefore, the physical meaning of the objective functions T_1 and T_2 are to make the overall structure isolate the vibration energy in the lower and wider frequency range on the premise of ensuring the structural stiffness as high as possible. The value of T_1 is generally much larger than 1, which means the fundamental frequency of the overall structure is far lower than the central frequency of the first band gap of the substructure.

In this paper, an improved GA and the FEM are used to optimize the coupling topology of cantilever beam support and vibration isolation in the example. The improved GA is used to perform the evolutionary iteration of design variables, and the FEM is used to solve the objective function values corresponding to each feasible substructure.

In the process of solving band structures of the substructure by FEM, periodic boundary conditions should be added at the interface of adjacent cells on the cantilever beam based on Bloch theorem of periodic structure [85], and the wave vector on the first irreducible Brillouin zone (Fig. 2a) of one-dimensional periodic structure should be scanned.

3. The improved multi-objective GA

GA [64] imitates the selection, crossover and mutation of chromosome genes in nature. When using GA for structural topology optimization, the 0~1 mesh matrix of the substructure needs to be transformed into the corresponding 0~1 binary coded chromosome gene row vector line by line, and the number of coding bits corresponds to the number of elements of the substructure mesh matrix. However, using the traditional GA to optimize the topology of the structure described in this paper will encounter the following problems:

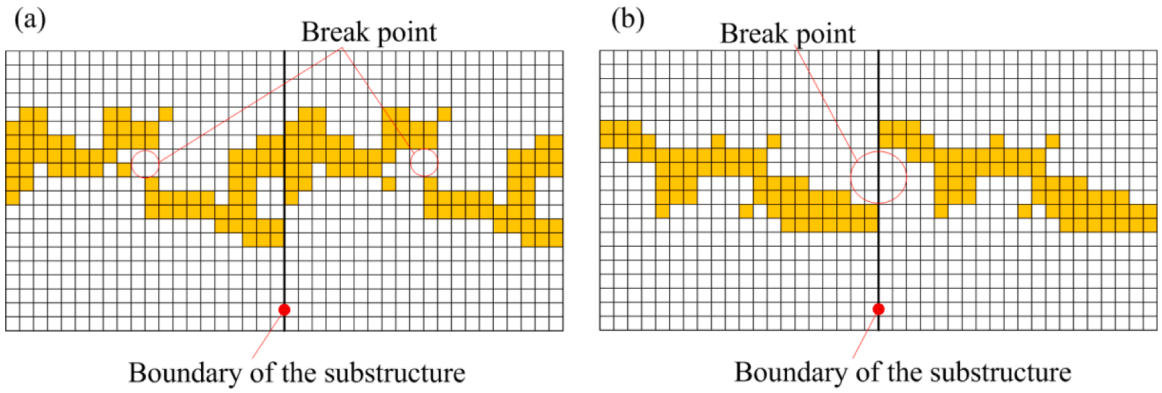

Fig. 3. (color online) Meshes of two different kind of island substructures: (a) island substructure with break point inside itself; (b) island substructure with break point on the edge of two substructures. The yellow squares are the real meshes.

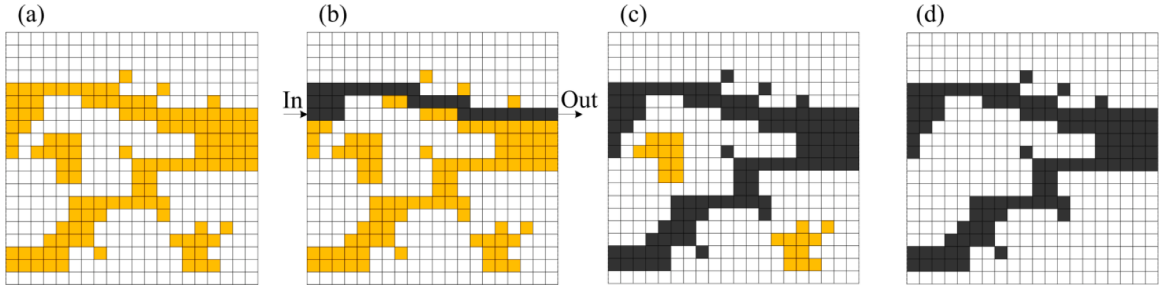

Fig. 4. (color online) Subsequent processing method of substructure meshes generated by GA: (a) initial mesh generated by GA; (b) finding the first continuous real mesh path (shown as the black squares) by maze algorithm from the input point to the output point; (c) searching for the remaining valid real meshes connected to the maze path, the two regions of yellow squares are the island real meshes; (d) island real meshes is eliminated.

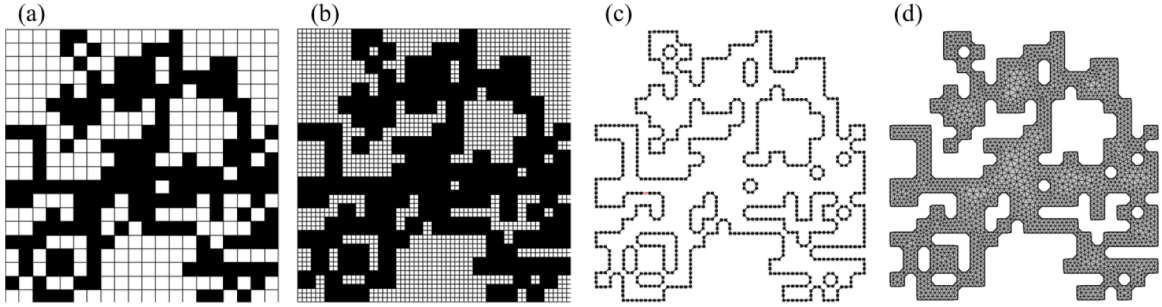

Fig. 5. Schematic diagram of several mesh states experienced by the substructures: (a) a relatively small number of meshes for valid individual search by GA; (b) meshes refinement of the 0~1 square mesh for smooth geometric boundary shape; (c) delete the internal meshing grids in the geometric contour of the effective real mesh area; and (d) re-mesh the area in the geometric contour by the free meshing program.

(a) Computing a large number of invalid population individuals causes a waste of computing resources and slows down the convergence speed.
(b) The number of meshes of substructures leads to the contradiction between the speed of operation and the quality of topology results.
(c) The inherent defects of traditional GA are the oscillation of objective function value at the end of evolution and the poor ability to search feasible solutions. Both of these are caused by the evolution of all population individuals with the same mutation rate and crossover rate.

In order to solve the above problems, this paper takes measures such as eliminating invalid population individuals, mesh generation strategy combing coarse mesh and fine mesh, regulating the crossover rate and variation rate of individuals and so on.

3.1. Elimination of invalid individuals before calculation

Without intervention, affected by the random search characteristics of GA, some individuals (0~1 mesh matrix of substructures) that do not meet the continuity requirements of cantilever beam and are not beneficial to the iterative process will be generated during the initialization and subsequent evolutionary iterations of the algorithm. These invalid individuals will lead to two problems when they are mixed into the evolutionary population. Firstly, invalid individuals will waste the population size and reduce the number of effective individuals in the population, which will affect the convergence speed. Secondly, the invalid individual will waste the time of solving the corresponding objective function value of the corresponding individual by the FEM. Therefore, it is necessary to judge the availability of the new individual searched by GA before entering the iterative population and solving the objective function value. Only the individuals determined to be valid

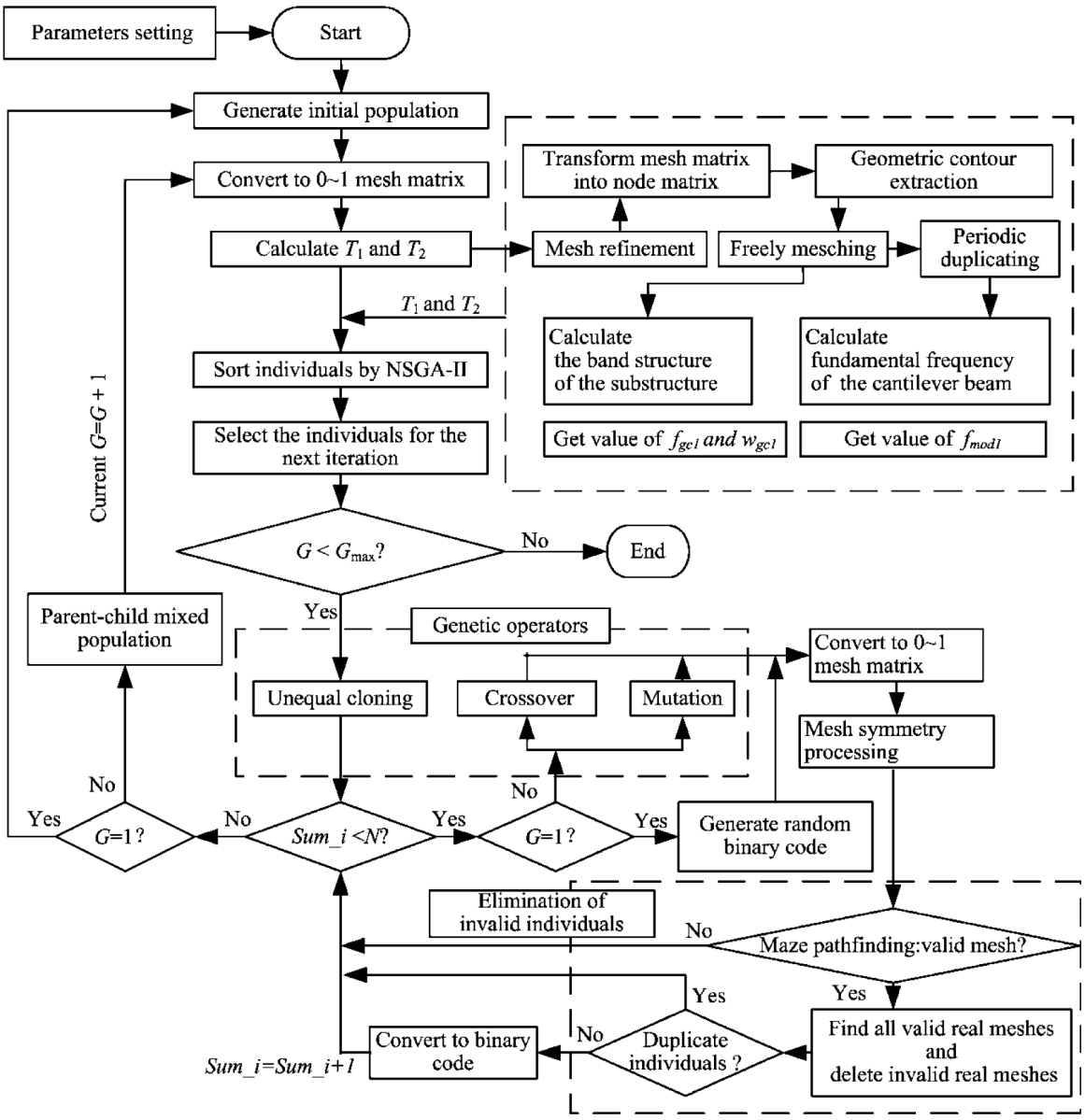

Fig. 6. Detailed algorithm flow: *Sum_i* indicates the total number of currently obtained valid individuals; *N* is the individual number of the parent population and also the offspring population; *G* is the current generation; *G*max indicates the max specified number of evolutional generations.

and subjected to the necessary mesh transformation can enter the iterative population. On the contrary, the individuals determined to be invalid will be eliminated in advance.

3.1.1. Maze path-finding and island individual elimination

The first step is to determine whether the newly found substructure individual by GA is an island individual. The beam structure formed by the periodic arrangement of the substructures must meet the overall stiffness index of the beam itself as the supporting structure. For this reason, the region in which the material is retained in the substructure must meet the condition of real mesh continuity along the length of the cantilever beam: firstly, there must be a path composed of continuous real mesh ($x = 1$) between the periodic boundaries on both sides of the substructure; secondly, the continuous real mesh path in the substructure should be able to continuously connect the real mesh path in its adjacent substructure. If there is no real mesh path in the substructure that meets the above requirements, the real mesh of the substructure will exist as discrete 'island'. After periodic one-dimensional layout, these substructures cannot form a continuous integral beam structure, which means that it will absolutely not meet the support function of the structure and cannot be actually manufactured, as shown in Fig. 3.

In order to judge whether the newly discovered substructure individual is an island individual or a continuous individual, the maze algorithm is introduced to find the continuous real mesh path in its 0~1 mesh matrix. Specifically, the 0~1 mesh matrix of the substructure is regarded as a maze. According to the characteristics of the beam structure, the entrance of the maze shall be located in the real mesh $x_{i1} = 1$on the first column of the substructure mesh, and the exit of the maze shall be located in the real mesh $x_{jn} = 1$on the last column of the substructure mesh. It should satisfy $-1 \ll i - j \ll 1$to ensure that the exit real mesh of the front substructure and the entrance real mesh of its next adjacent substructure shall be connected through at least one node, so as to ensure that the substructures after periodic replication and arrangement form a continuous cantilever support structure. The maze algorithm based on recursive backtracking is used to search the continuous path of real mesh from $x_{i1} = 1$ to $x_{jn} = 1$of the substructure mesh maze.

Once the first maze path is found (there may be other feasible paths), the search is stopped to reduce the computational cost, and the

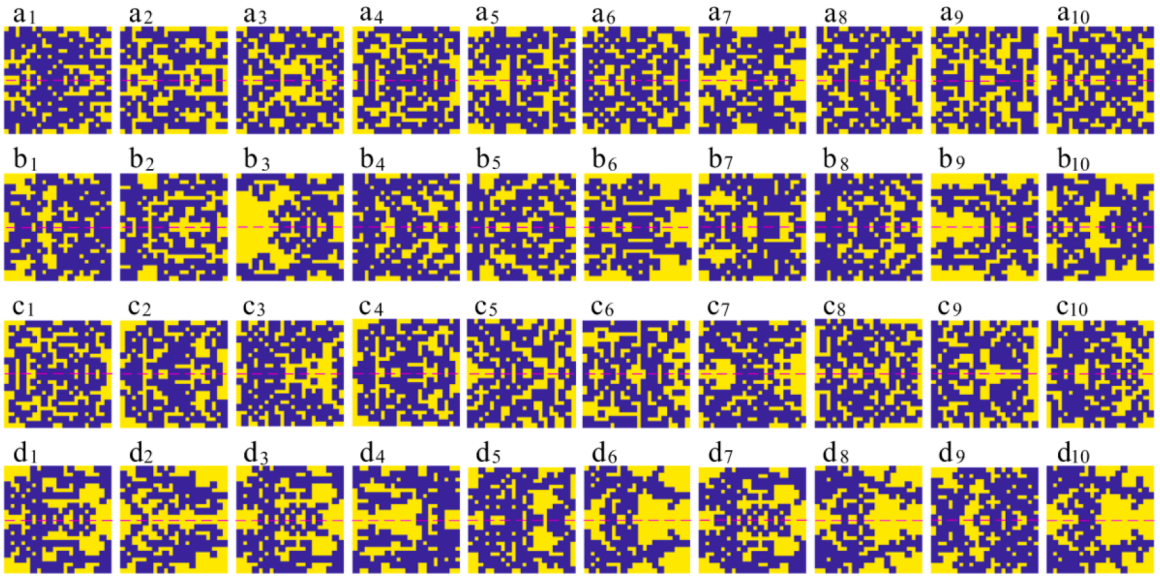

Fig. 7. (color online) Substructures with transverse symmetry constraints corresponding to the top 10 individuals obtained by two different algorithms: substructures from a_1 to a_{10} and substructures from c_1 to c_{10} are obtained by the original NSGA-II algorithm at the initial and the 30th generation respectively; substructures from b_1 to b_{10} and substructures from d_1 to d_{10} are obtained by the proposed algorithm at the initial and the 30th generation, respectively. The dotted line in each subgraph is the axis of symmetry.

Table 1
Global invariant parameters used in the example.

Symbols	Parameter type	Parameter value
E	Young's modulus	110e9 [Pa]
ρ	Material density	4440 [Kg/m^3]
p_r	Poisson's ratio	0.35
a	The length of the substructure	0.05[m]
b	The width of the substructure and the cantilever beam	a
L	The length of cantilever beam	5*a
m_a	Number of columns of substructure mesh adopted by GA	20
m_b	Number of rows of substructure mesh adopted by GA	20
m_f	Mesh refinement multiplier for optimizing substructure topology contour	3
N	Individual number of the parent population and also the offspring population	80
$G_{\max}$	Maximum evolutional generation	80
C_p	Crossover rate of selected parents	0.5
M_{pmin}	The minimum mutation rate of gene of selected individuals	0.1
M_{pmax}	The maximum mutation rate of gene of selected individuals	0.4

individual is judged to be valid, as shown in Fig. 4. If no feasible path is found after all explorations is completed, the individual is judged as an island individual and should be eliminated.

3.1.2. Remaining valid real meshes search and invalid island real meshes deletion

After finding the above individuals with valid maze paths, other valid real meshes connected to the maze paths also need to be found in the individual 0~1 mesh matrix. As shown in Fig. 4, explore the area near the maze path in turn, find other real meshes that share at least one mesh node with the real meshes in the maze path, and include these qualified real meshes in the real meshes set of the maze path. Then, the search is repeated until all valid real meshes are added to the real mesh set of the maze path to maximize its area. After the search cycle of valid real meshes is completed, there may be some residual island real meshes outside the real meshes set of the maze path. These island real meshes have no contribution to the overall structural stiffness of the cantilever beam. If not handled, these useless island real meshes will always iterate with the topology process, aggravating the chessboard phenomenon of the topology mesh. In addition, the island real mesh in the valid individuals participating in the evolutionary iteration will not be conducive to identifying the effective differences between different individuals (the differences between the maximum area maze paths of different individuals). The existence of island real mesh will also affect the judgment of whether the new individual is different from the existing individual. If two individuals differ only in the distribution of island real grid outside the maximum area maze path, they should not be regarded as different individuals, otherwise it will lead to useless eigenvalue solving operation. In view of the above reasons, this paper converts the remaining island real meshes ($x = 1$) into virtual meshes ($x = 0$), as shown in Fig. 4(d).

3.1.3. Making the individuals in the population different from each other

After finding the above individual with valid mesh and modifying its 0~1 mesh matrix, it is necessary to further confirm whether the new individual is really new, that is, whether it is different from all other existing valid individuals in current generation. To be recognized as a real new individual, the individual must have at least one difference on its valid real mesh from that of all individuals in the current parent population and the already generated offspring population. Otherwise, the individual is a duplicate individual.

If the population contains duplicate individuals, the diversity of the population will be reduced, especially near the end of evolution. In extreme cases the number of individual species in the population is one. Worse, the program of FEM needs to repeatedly calculate the objective function value of the same individual. Not only these repeated operations are meaningless, but also they are easy to fall into local convergence due to poor population diversity, and cannot obtain the global optimal topological substructure. Therefore, the duplicate individuals should be eliminated as invalid individuals.

Therefore, this paper judges and excludes the above invalid individuals in many places in the algorithm, and realizes the elimination of invalid individuals before calculation, so as to maintain the diversity of the population and save computing resources. See the algorithm flow chart in Fig. 6 for the specific timing of invalid individual judgment and elimination.

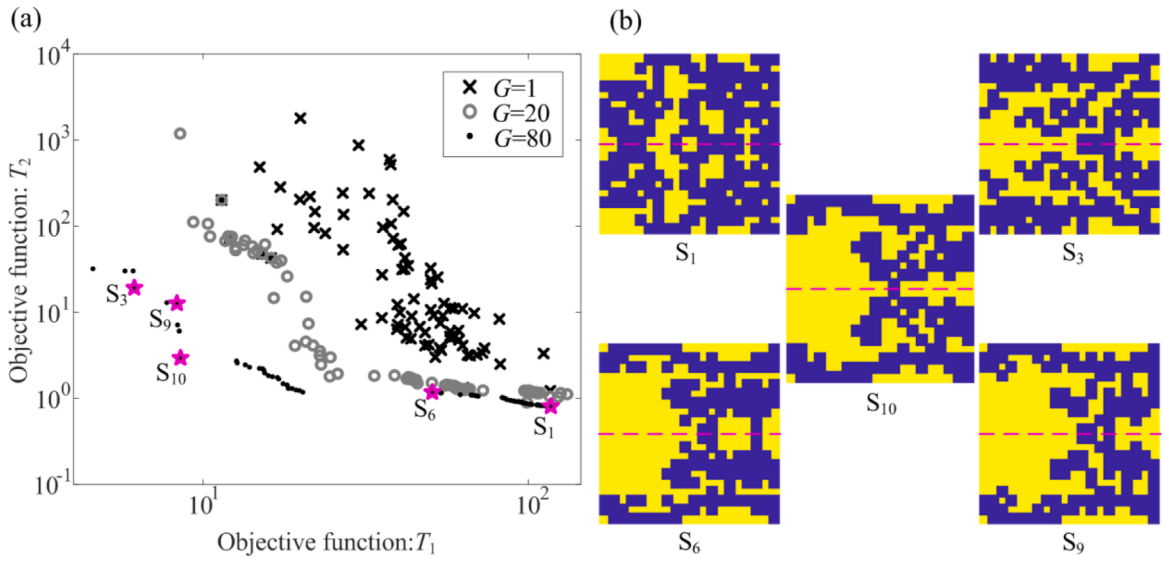

Fig. 8. (color online) (a) The two objective function values T_1 vs. T_2 of the individuals in the populations corresponding to evolutionary generations $G = 1$, 20 and 40, and (b) the five representative individuals, S_1, S_9, S_{10}, S_6 and S_1 of the 80th generation which marked in subgraph (a). The dotted line in each subgraph is the axis of symmetry.

Table 2
More information of the five individuals of the 80th generation with transverse symmetry constraints.

Substructure	T_1	T_2	f_{mod1} [Hz]	f_{gs1} [Hz]	f_{ge1} [Hz]	f_{gc1} [Hz]	w_{gp1} [Hz]	v_f
S_3	6.1	19.2	189	1134	1195	1164.5	60	46%
S_9	8.3	12.7	276	2204	2385	2294.5	180	37%
S_{10}	8.5	2.9	310	2196	3093	2644.5	897	39%
S_6	50.6	1.2	118.6	3461	8549	6005	5088	40%
S_1	117.1	0.8	127	5715	24,190	14,952	18,475	57%

3.2. Mesh generation strategy combining coarse mesh and fine mesh

If the meshes are divided too finely, it will lead to more design variables and the GA will be slow to search for high-quality individuals, but it can obtain better objective function. On the contrary, if the meshes are divided too coarsely, it is difficult to converge to a better topological structure, although the design variables are fewer and the calculation speed is faster.

In order to alleviate the above contradictions, in the algorithm flow of this paper, a three steps of meshing operation with different mesh sizes is set up between topologically generating the substructure configuration and executing the FEM program to solve for the objective function value, as shown in Fig. 5, including:

(a) The 0~1 mesh variable matrix used by GA.
(b) Mesh refinement before importing substructure configuration into finite element software.
(c) Freely meshing of the substructure though finite element software.

Firstly, as mentioned above, when using GA to search for valid substructure individuals, a square mesh with four nodes is used, which represents the presence or absence of materials at the corresponding positions in the substructure. At this stage, a relatively small number of meshes are set to reduce the search space for valid individual search by GA and improve the speed of topology design, as shown in Fig. 5(a). In order to find as many valid real meshes as possible in a limited number of four node square mesh matrices, as mentioned earlier, the condition for judging the continuity of real meshes is that there is at least one common node between the two real meshes. However, this continuous structure realized by a single common node is difficult to manufacture, and will affect the solution result of the objective function. Therefore, before importing the substructure after GA topology into the finite element software, it is necessary to further refine the 0~1 square mesh matrix of the substructure, so as to change single-node connection to multi-nodes connection and make the geometric boundary shape of the substructure smoother, as shown in Fig. 5(b). After the above processing, only the geometric contour of the effective real mesh area of the substructure is retained, and the internal meshing is deleted, as shown in Fig. 5(c). Then the geometric contour of the substructure is imported into finite element software, and the area in the geometric contour is re-meshed by the free meshing program. The advantage is that any FE software program can automatically select the mesh size according to the complexity of the local structure in the substructure, so as to automatically adjust the total number of DOF of the meshes to the best during the finite element solution, so as to improve the solution speed, as shown in Fig. 5(d).

3.3. Regulation of crossover rate and mutation rate

Crossover and mutation are two basic operators of the traditional GA. The probability of using these two operators is controlled by setting the parameters of crossover rate and mutation rate. It is important to understand that these two parameters do not refer to the probability of an individual in the parent population being selected to perform crossover or mutation operations, but the probability that a mutation or crossover operation will occur for each variable of the randomly selected individual from the parental population. In traditional GA, these two parameters are usually set to be global invariant. In the later stage of iteration, the same mutation rate is used for individuals with better and worse objective function values, which is not conducive to the local search convergence of high-quality individuals and the rapid evolution

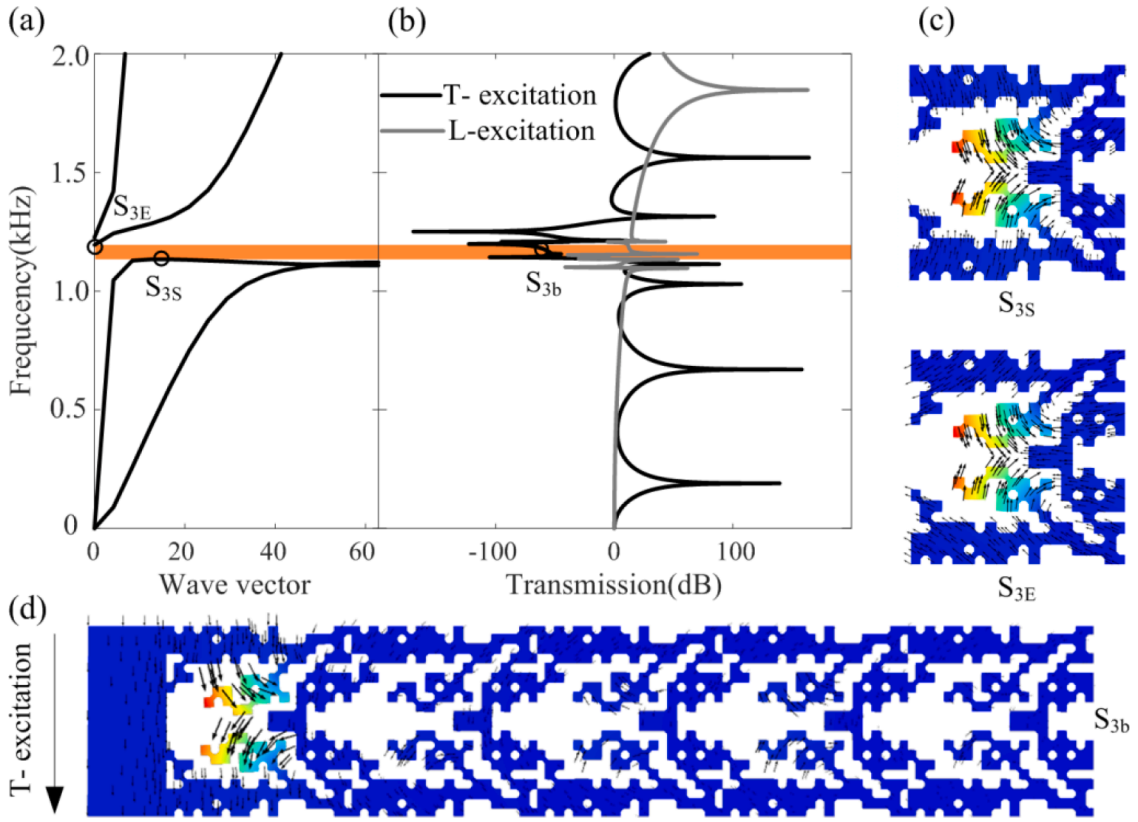

Fig. 9. (color online) Relevant calculation results of substructure S_3. (a) The band structure, (b) the transfer function curves of corresponding cantilever beam under transverse excitation (T-excitation) and longitudinal excitation (L-excitation), (c) the eigenmodes S_{3S} and S_{3E} labeled in the band structure, and (d) cantilever vibration mode S_{3b} under T-excitation inside the band gap frequency range.

of low-quality individuals.

Therefore, the mutation rate controlled by the ranking of individual objective function values is adopted, which means that when the mutation operation is performed on the randomly selected individuals, the 0∼1 transformation probability of each mesh variable is composed of a basic minimum mutation rate and a adjusted mutation rate, which can be defined as:

$$M_p(i) = M_{pmin} + \frac{i}{N} \times \left(M_{pmax} - M_{pmin}\right) \tag{2}$$

where $M_p(i)$is the mutation rate for variables of the ith individual in the population sorted from good to bad according to the objective function value; M_{pmin} and M_{pmax} are the minimum and maximum variation rate of each variable in the selected individual respectively; N is the total number of individuals in the population. It can be seen that low-quality individuals with lower ranking have higher probability of gene mutation, which improves the opportunity for individuals to produce high-quality individuals, and thus improves the ability to avoid the optimization search falling into the local optimal solution; On the contrary, the high-quality individuals in the top rank have a small probability of gene mutation. They can slightly change the mesh on the basis of the original high-quality mesh distribution to speed up the convergence.

In addition, the population individuals of traditional GA gradually converge to a small number of species with the increase of evolutionary generation, resulting in the gradual increase of duplicate individuals in the population and the gradual decrease of population diversity. Therefore, as mentioned above, the method of eliminating duplicate individuals is adopted to make individuals in the parental population and offspring population different from each other in order to ensure the population diversity and avoid performing finite element solutions for identical individuals. However, the population without duplicate individuals has a problem that the quality individuals in the population do not obtain a higher probability of being randomly selected when crossover and mutation operations are performed. In order to make up for the above shortcomings, unequal cloning operations were adopted for all parental individuals before crossover and mutation operations. According to the ranking of individual objective function values from good to bad, the copy number of corresponding parent individuals is from more to less, so as to improve the probability of selecting high-quality individuals for crossover and mutation operations. Please note that unequal cloning will not affect the diversity of the population, because the individuals in the parent population participating in the current evolutionary process are different from each other in the initial state.

3.4. Algorithm flow

In order to realize multi-objective optimization, the above improvements are based on the NSGA-II [64]. Combined the FEM and the improved NSGA-II which is mentioned above, the detailed algorithm flow for the coupling topology optimization of vibration isolation and structural support of the cantilever beam is shown in Fig. 6.

The main steps of the algorithm flow are determined as follows:

(a) The global invariant parameters for invocation by the main program and its subroutines are defined, including: substructure size, cantilever beam size (number of its substructures), material parameters, meshing related parameters and GA related parameters.
(b) Through valid individual search and duplicate individual elimination, the initial population of individuals with different substructures is obtained.

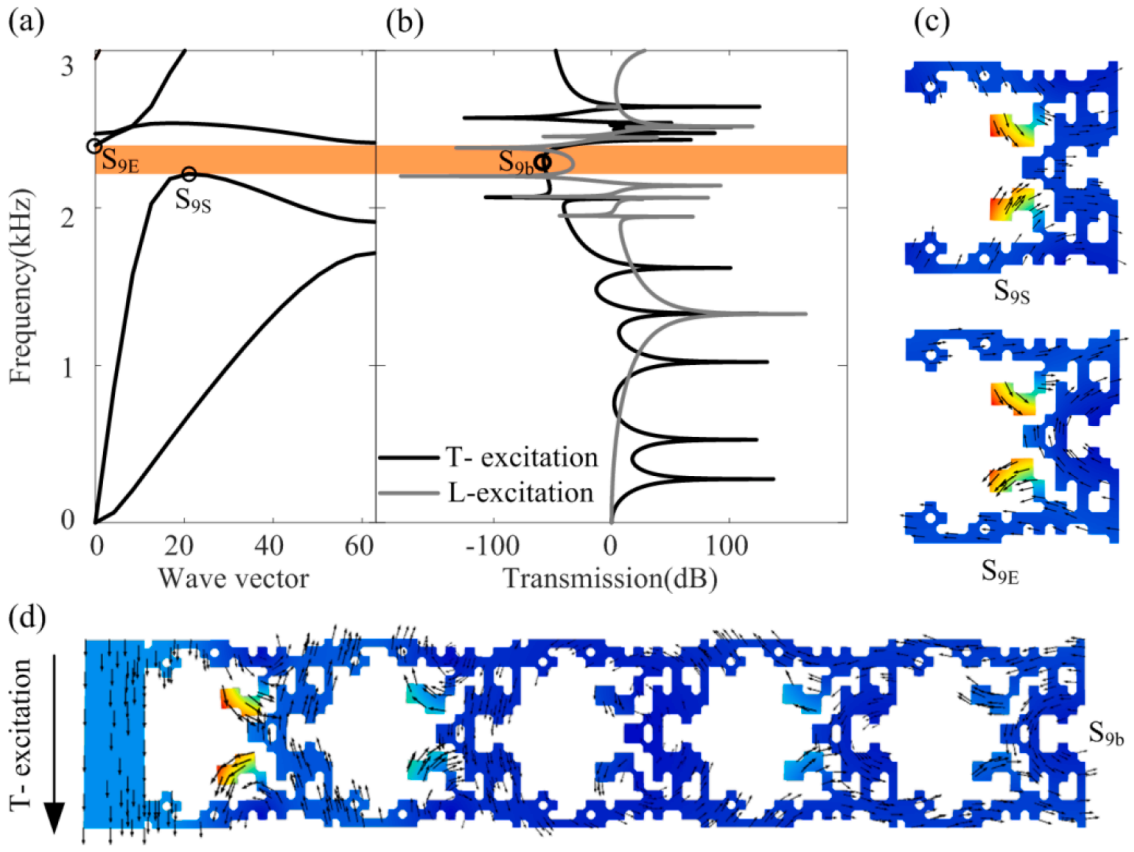

Fig. 10. (color online) Relevant calculation results of substructure S_9. (a) The band structure, (b) the transfer function curves of corresponding cantilever beam under transverse excitation (T-excitation) and longitudinal excitation (L-excitation), (c) the eigenmodes S_{9S} and S_{9E} labeled in the band structure, and (d) cantilever vibration mode S_{9b} under T-excitation inside the band gap frequency range.

(c) The geometric contour of the substructure is optimized and adjusted through mesh refinement, and the refined mesh matrix is transformed into node matrix, which is imported into finite element software, and the area in the geometric contour is re-meshed by the freely meshing program of the software. Then the band structure solution and band gap identification of the substructure are carried out to obtain the center frequency value f_{gc1} and the gap width $w_{gc1}$of the first band gap. The substructures are arranged in a one-dimensional array, and fixed constraints are imposed on the starting end boundary to obtain the finite element model of the cantilever beam with periodic structure characteristics, and then its vibration mode solution is carried out to obtain the fundamental frequency f_{mod1}. So far, the objective function values T_1 and T_2 of the substructure are obtained; The objective function values of all individuals in the population are calculated in turn.

(d) The individuals of the population are sorted by NSGA-II, and the individuals entering the next iteration are selected according to the sorting results.

(e) Start the genetic evolution iteration. Firstly, unequal cloning is carried out according to the order of individuals in the population. One individual was randomly selected from the cloned parent population for mutation, and two parent individuals were randomly selected for crossover. If the offspring individuals obtained through crossover or mutation are determined to be valid and non-repetitive, they will be included in the offspring population. *Sum_i* indicates the total number of currently obtained valid individuals. Perform the above steps one by one until the required number of offspring individuals are obtained. Call the finite element software to calculate the objective function value corresponding to each offspring individual according to the same operation as step (c).

(f) The parent population individuals and the offspring population individuals both with objective function value attributes are mixed to form a mixed population. The individuals of the mixed population are sorted by NSGA-II, and a specified number of high-quality individuals are selected as the parent population of the next generation.

(g) (g) According to the above steps, the specified number of evolutional generations G_{max} are completed in turn to obtain the final topological configuration of the substructure, and then the operation is terminated.

3.5. *Effectiveness of the algorithm improvement*

In order to briefly illustrate the effectiveness of the proposed algorithm and its improvement on the search process, the proposed algorithm and the original NSGA-II algorithm are used to calculate the same example proposed in this paper, and the top 10 individuals of the initial and the 30th generation population obtained by the two algorithms are compared, as shown in Fig. 7. The values of parameters used in calculation are shown in Table 1.

Due to the lack of continuity constraints on materials in the algorithm, discontinuous island real meshes can be found in most substructures obtained by the original NSGA-II algorithm, which still exists in the individuals of the 30th generation population. And some individuals, such as a_5 and c_9, do not even have a continuous force transmission path along the length of the beam. Moreover, even after 30 generations of evolution, the material distributions of these structures are still relatively scattered, which are reflected in more complex shapes and more pores, and increase the manufacturing difficulty. The

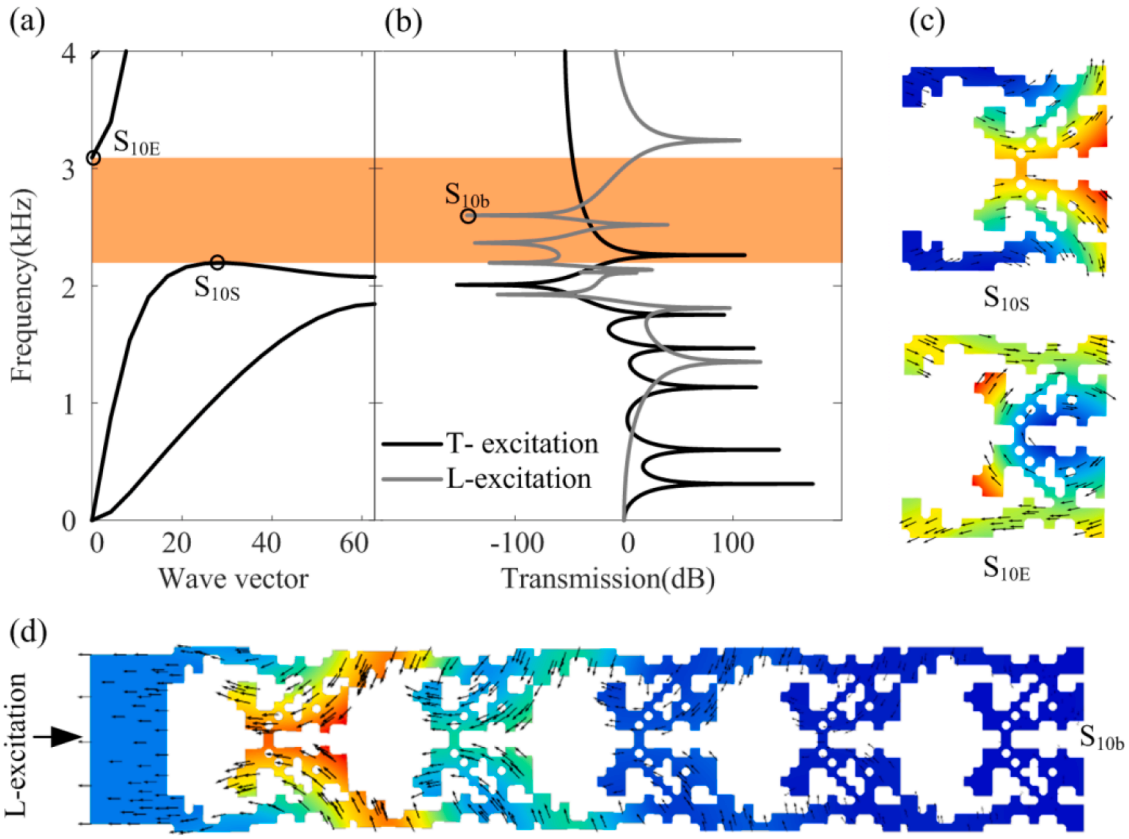

Fig. 11. (color online) Relevant calculation results of substructure S_{10}. (a) The band structure, (b) the transfer function curves of corresponding cantilever beam under transverse excitation (T-excitation) and longitudinal excitation (L-excitation), (c) the eigenmodes S_{10S} and S_{10E} labeled in the band structure, and (d) cantilever vibration mode S_{10b} under L-excitation inside the band gap frequency range.

optimization results obtained by our proposed algorithm with manufacturability constraints can effectively avoid the above situations and effectively improve the availability of optimization results. The individuals obtained by the proposed algorithm have clearer and stronger force transmission paths, reflecting more effective material utilization. In addition, comparing the results of the 30th generation, it can be found that the proposed algorithm converges faster. Substructures obtained by the proposed algorithm converge to six configurations (substructures d_6, d_8 and d_{10} are one kind of configuration, substructures d_1, d_3 and d_7 are the other kind of configuration, and the rest substructures each have different configurations), while the substructures obtained by the original NSGA-II algorithm are almost different from each other.

Through the above simple comparisons, it can be seen that compared with the original NSGA algorithm, the substructures searched by the proposed algorithm in this paper is more reasonable in the utilization of materials, which ensures the continuity of the overall structure composed of the substructures, avoids invalid eigenvalue solution by excluding unreasonable individuals, and speeds up the convergence speed of operation. Due to the limitation of space and topic, this paper will not carry out a more in-depth analysis of the proposed algorithm.

4. Optimization results and analysis

4.1. Parameter setting

The values of global parameters used in the cantilever beam example in this paper are shown in Table 1.

4.2. Multi-objective calculation results with transverse symmetry constraints

According to the above parameter settings, firstly, the situation when transverse symmetry constraints are applied to the topological features in the substructure is analyzed. Fig. 8 shows the distribution of objective function values T_1 and T_2 of individuals in the population corresponding to some evolutionary generation G. As can be seen from Fig. 8(a), the distribution of objective function values of initial population ($G = 1$) individuals has good diversity. With the increase of evolutionary generation, the two objective function values gradually converge to a local Pareto front. The five representative individual substructures under the maximum evolutionary generation ($G = 80$) are singled out from the local Pareto front. Table 2 gives more comprehensive calculation result information corresponding to these five individuals, where v_f is the volume fraction of real mesh in the $n \times m$ mesh matrix of the substructure, f_{gs1} and f_{ge1} are the start frequency and end frequency of the first-order complete vibration band gap, respectively.

Compared from the topological shape, the five substructures ranking No. S_1, S_3, S_6, S_9 and S_{10} have a certain degree of similarity. For example, substructure S_3 extends out of a local cantilever structure in the direction of its symmetry line. Substructure S_9 inherits the local cantilever structure characteristics of substructure S_3, but its pore structure is less, and the material concentration of continuous structure is better, so its lightweight degree is higher. Substructures S_{10} and S_6 have a volume fraction similar to that of substructure S_9. Compared with substructure S_9, the two local cantilever structures of substructure S_{10} near the symmetry line is connected through real meshes to shorten the cantilever of the local structure. Compared with substructure S_{10}, substructure S_6 spans the symmetry line to increase the number of channels connected up and down. Compared with other four substructures, the

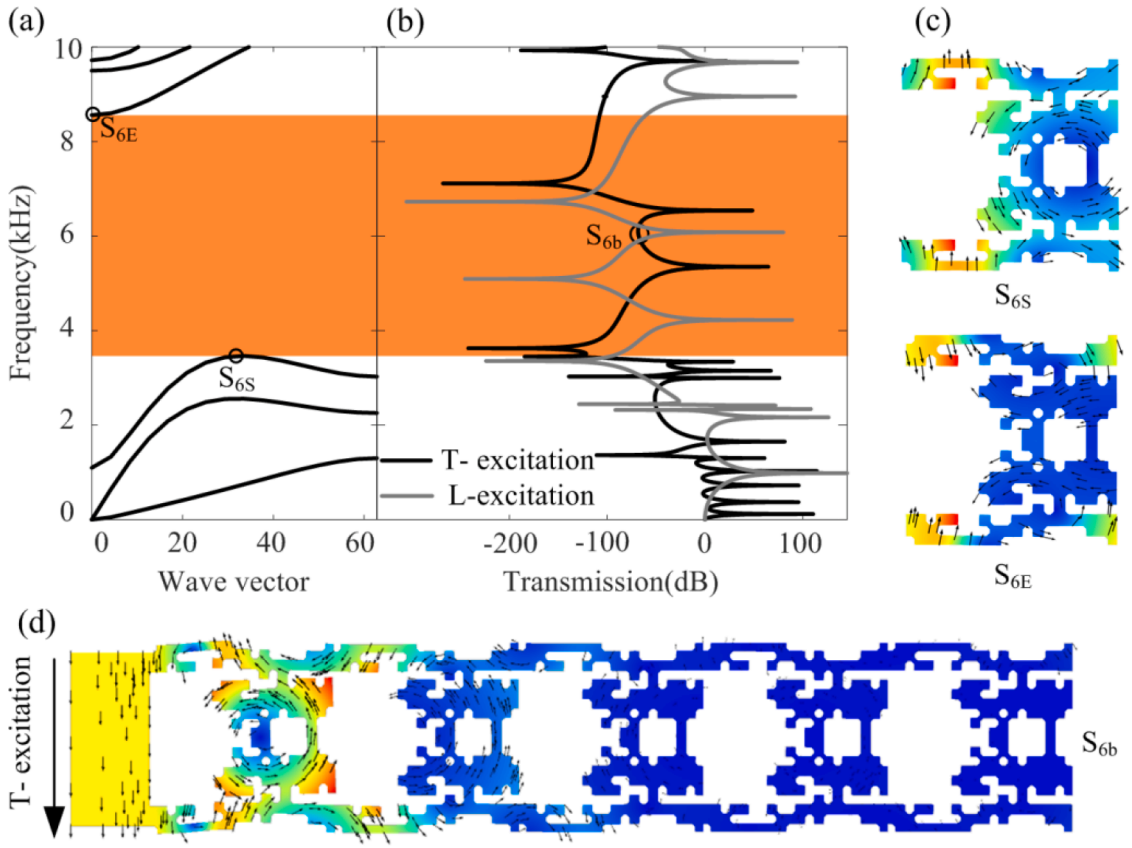

Fig. 12. (color online) Relevant calculation results of substructure S_6. (a) The band structure, (b) transfer function curves of corresponding cantilever beam under transverse excitation (T-excitation) and longitudinal excitation (L-excitation), (c) the eigenmodes S_{6S} and S_{6E} labeled in the band structure, and (d) cantilever vibration mode S_{6b} under T-excitation inside the band gap frequency range.

difference of substructure S_1 is more obvious. Its lightweight degree (v_f = 57%) is the worst among the five substructures, the connection between the upper and lower symmetrical parts is the most, and there are obvious differences in the outer contour dimensions in the width direction of the cantilever beam.

It can be seen from the data listed in Table 2 that the T_1, w_{gp1}, f_{gc1} and f_{ge1} increase in order of substructure S_3, S_9, S_{10}, S_6, S_1, the f_{gs1} is basically compounded with this law. While T_2 decreases in order of substructure S_3, S_9, S_{10}, S_6, S_1. The distribution law of the fundamental frequency of the whole cantilever structures corresponding to each substructure is not obvious, which is due to the larger fluctuation range of the function value related to the band gap and its more significant impact on the topological trend.

Relevant calculation results of the five substructures are showed in Figs. 9–13. The first band gap of substructure S_3 appears between the 2nd band and the 3rd band, and the 2nd band contains a relatively straight curve segment. As can be seen from Fig. 9(b), when one end of the cantilever composed of substructure S_3 is transversely excited, the response amplitude of the free end of the cantilever relative to the input end is significantly reduced within the band gap frequency range shown in Fig. 9(a), which proves the existence of the band gap and the vibration suppression effect of the band gap. According to the substructure modal shapes corresponding to the band gap start frequency and end frequency shown in Fig. 9(c) and the vibration mode of the cantilever beam corresponding to point S_{3b} on the transverse excitation transfer function curve shown in Fig. 9(d), the main vibration energy is localized in the swing movement of the local cantilever structure, and the vibration propagation on the simplest continuous path of the front and rear substructures is weakened. Further, combined with the characteristics of narrow band gap width and low band gap center frequency, it can be judged that the band gap is a local resonance band gap.

The first band gap of substructure S_9 also appears between the 2nd band and the 3rd band, but there is no relatively straight curve segment contained in the 2nd band. As can be seen from Fig. 10(b), when the cantilever composed of substructure S_9 is subjected to transverse excitation and longitudinal excitation respectively, the amplitude of the transfer curves of the cantilever both decrease within the frequency range corresponding to the band gap shown in Fig. 10(a), which proves the existence of the band gap. According to the substructure modal shapes corresponding to the band gap start frequency and end frequency shown in Fig. 10(c) and the vibration mode of the cantilever beam corresponding to S_{9b} point on the transverse excitation transfer function curve shown in Fig. 10(d), part of the vibration energy is still localized in the local cantilever branch inside the substructure. However, compared with substructure S_3, the band gap width of substructure S_9 increases, the band gap center frequency moves upward, and part of the vibration energy within the vibration band gap frequency range is dispersed outside the local cantilever branch, that is, the localization degree of vibration energy in the band gap decreases. The main reason for these differences is that the length of local cantilever branches in substructure S_9 is shorter than that in substructure S_3.

The first band gap of substructure S_{10} also appears between the 2nd band and the 3rd band. As shown in Fig. 11(a), substructure S_{10} has a wider and higher first-order band gap. The displacement displayed by the modal shape S_{10S} corresponding to the band gap start frequency shown in Fig. 11(c) is mainly reflected in the length direction of the cantilever beam. Fig. 11(b) also shows that when the cantilever beam is longitudinally excited, its transfer curve decreases more obviously in the band gap frequency range. Fig. 11(d) shows the vibration mode S_{10b} of the cantilever beam when it is longitudinally excited with a frequency in the band gap. It can be seen that the vibration energy gradually attenuates from the input end to the output end, which proves the effective

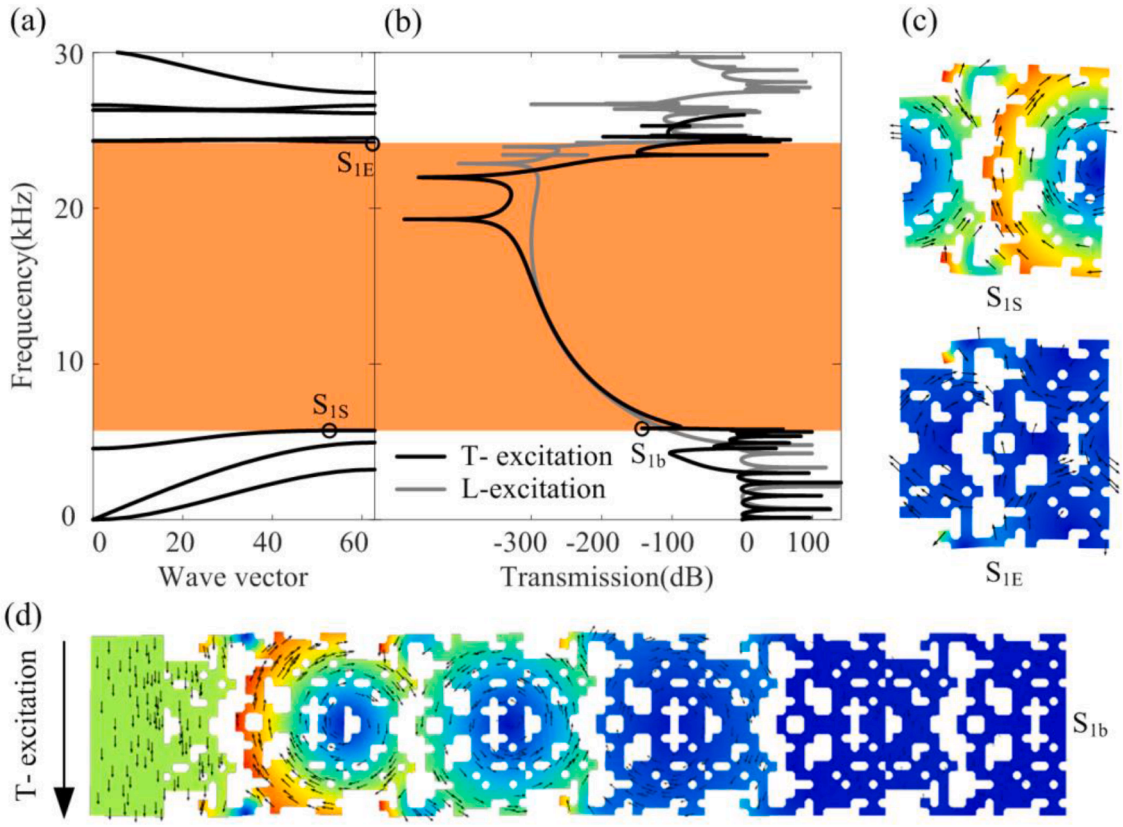

Fig. 13. (color online) Relevant calculation results of substructure S_1. (a) The band structure, (b) the transfer function curves of corresponding cantilever beam under transverse excitation (T-excitation) and longitudinal excitation (L-excitation), (c) the eigenmodes S_{1S} and S_{1E} labeled in the band structure, and (d) cantilever vibration mode S_{1b} under T-excitation inside the band gap frequency range.

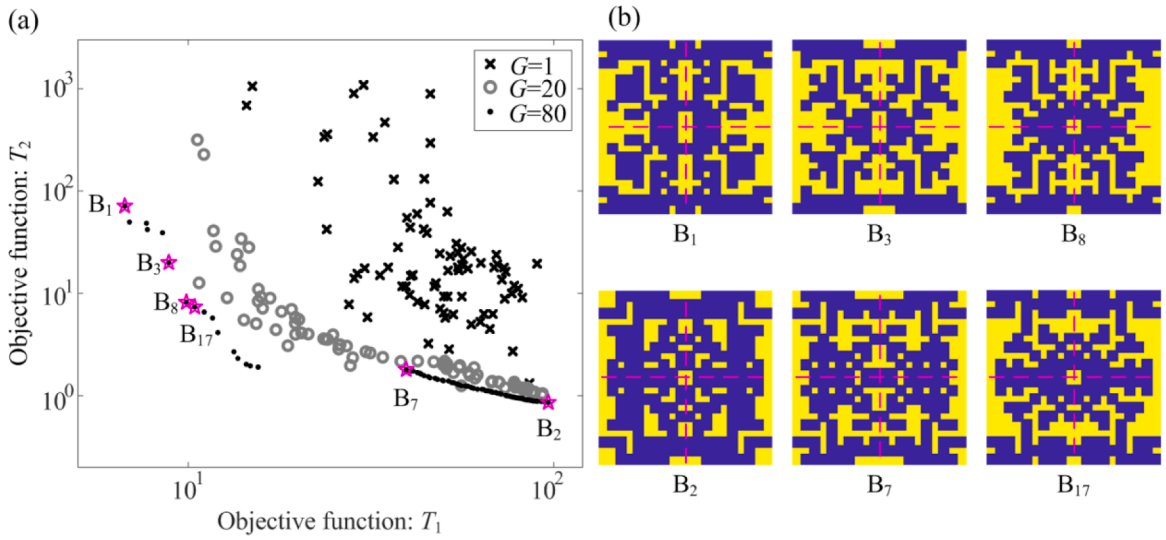

Fig. 14. (color online) (a) The two objective function values T_1 vs. T_2 of the individuals in the populations corresponding to evolutionary generations $G = 1$, 20 and 80, and (b) the six representative individuals, B_1, B_3, B_8, B_2, B_7 and B_{17} of the 80th generation which marked in subgraph (a). The dotted lines in each subgraph are the axis of symmetry.

isolation effect of substructure S_{10} on the longitudinal vibration excitation in the band gap. At the same time, from the distribution of the vibration energy of the mode of the band gap start frequency and the vibration mode of the cantilever beam, there is no obvious local resonance phenomenon. This is mainly because the cantilever branch inside the substructure is short, strong and rigid, which is difficult to arouse local resonance. Based on the above information, it can be judged that the first-order complete band gap of substructure S_{10} belongs to Bragg scattering band gap.

The first band gap of substructure S_6 shows more obvious Bragg scattering characteristics. As shown in Fig. 12(a), the band gap appears between the 3rd band and the 4th band, which is different from that of substructure S_3, S_9 and S_{10}. When the cantilever beam composed of substructure S_6 is transversely excited, except for two obvious resonance

Table 3
More information of the six individuals of the 80th generation with bisymmetry constraints.

Substructure	T_1	T_2	f_{mod1} [Hz]	f_{gs1} [Hz]	f_{ge1} [Hz]	f_{gc1} [Hz]	w_{gp1} [Hz]	v_f
B_1	6.7	71.4	348	2317	2349	2333	33	0.53%
B_3	8.9	20.0	252	2178	2290	2234	112	0.43%
B_8	9.9	8.2	277	2571	2905	2738	335	0.48%
B_{17}	10.4	7.4	218	2116	2424	2270	308	0.51%
B_7	39.5	1.8	160	4565	8075	6320	3511	0.50%
B_2	96.6	0.9	158	6391	24,095	15,243	17,704	0.60%

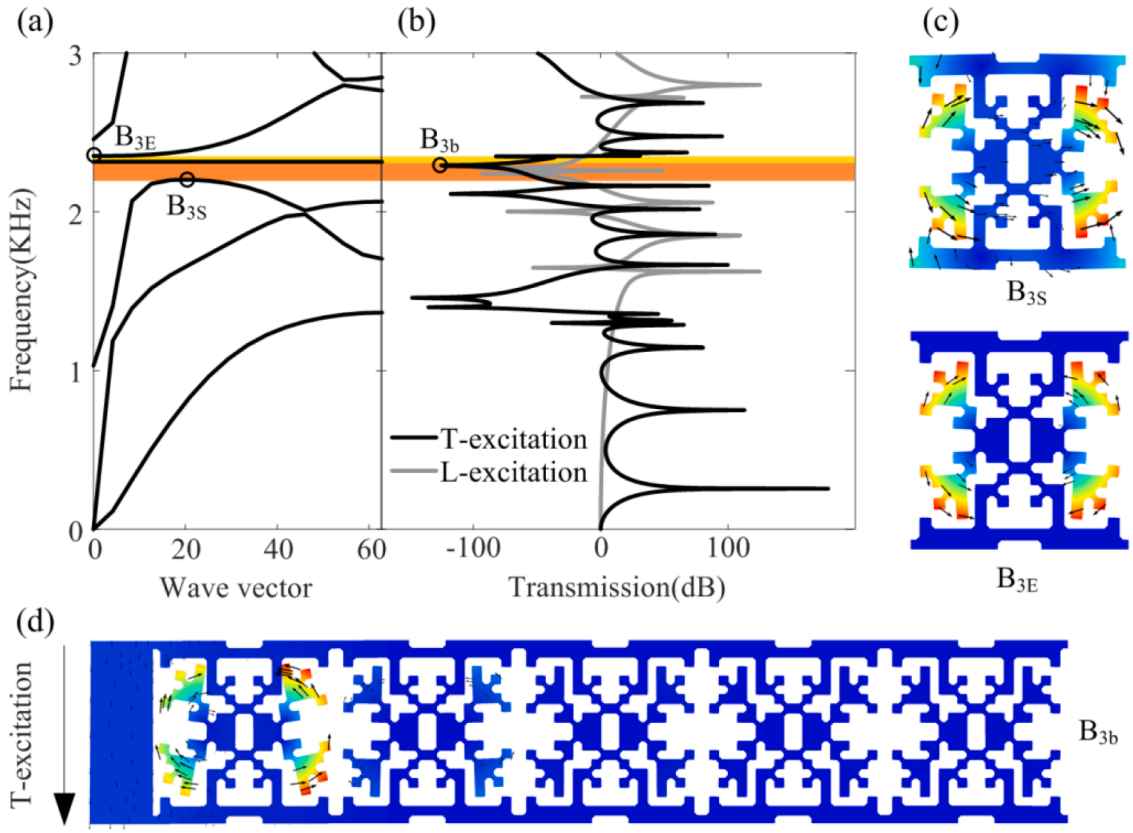

Fig. 15. (color online) Relevant calculation results of the substructure B_3 in the population of the 80th generation under bisymmetry constraints. (a) The band structure, (b) the transfer function curves of corresponding cantilever beam under transverse excitation (T-excitation) and longitudinal excitation (L-excitation), (c) the eigenmodes B_{3S} and B_{3E} labeled in the band structure, and (d) cantilever vibration mode B_{3b} under T-excitation inside the band gap frequency range.

peaks of the overall structure of the cantilever beam, the amplitude of the transfer curve has obvious attenuation within the band gap frequency range, as shown in Fig. 12(b). In addition, from the mode S_{6S} corresponding to the band gap start frequency, due to the increase of the connection path between the upper and lower cantilever branches in the substructure, the overall stiffness of the branch structure is improved, and the vibration response is more reflected in the weak link of the direct continuous path outside the branch structure. It can be found from the response mode S_{6b} of the cantilever beam of transverse excitation in the band gap that the vibration attenuation of the output end relative to the input end is very significant, and the vibration energy is greatly attenuated in the first two substructures.

Compared with the other four substructures, when the cantilever beam composed of substructure S_1 is subjected to transverse excitation and longitudinal excitation respectively, it both shows a very significant decrease in the response amplitude of the vibration transfer curve in the whole first band gap frequency range. As shown in Fig. 13(b), the maximum attenuation amplitude can reach more than 300 dB. The reason for the significant suppression effect on both transverse and longitudinal excitation can be found from the mode S_{1S} corresponding to the band gap start frequency. The two continuous solid areas with good stiffness and large mass in the front and rear parts of substructure S_1 are connected by longitudinal local thin beams. Under the mode S_{1S} shown in Fig. 13(c), the front and rear continuous entities rotate in reverse with an action similar to gear meshing, so that the energy transfer of longitudinal and transverse vibration is suppressed by transforming longitudinal and transverse vibration into reverse rotation motion in the substructure. Fig. 13(d) shows the trend that the vibration energy gradually decreases along the length of the cantilever beam when subjected to transverse excitation in the band gap frequency range. This band gap also has significant Bragg scattering characteristics.

Based on the above numerical simulation results under transverse symmetry constraints, the objective function T_1 protects the overall stiffness of the cantilever beam and makes the calculation result develop to a lower and narrower local resonance band gap, while the objective function T_2 makes the topological result tend to a wider and higher Bragg scattering band gap. As the objective function values of the individuals change from the best T_1 to the best T_2, the band gap characteristics of the individuals reflect the transformation trend from local resonance type to Bragg scattering type. The connection and

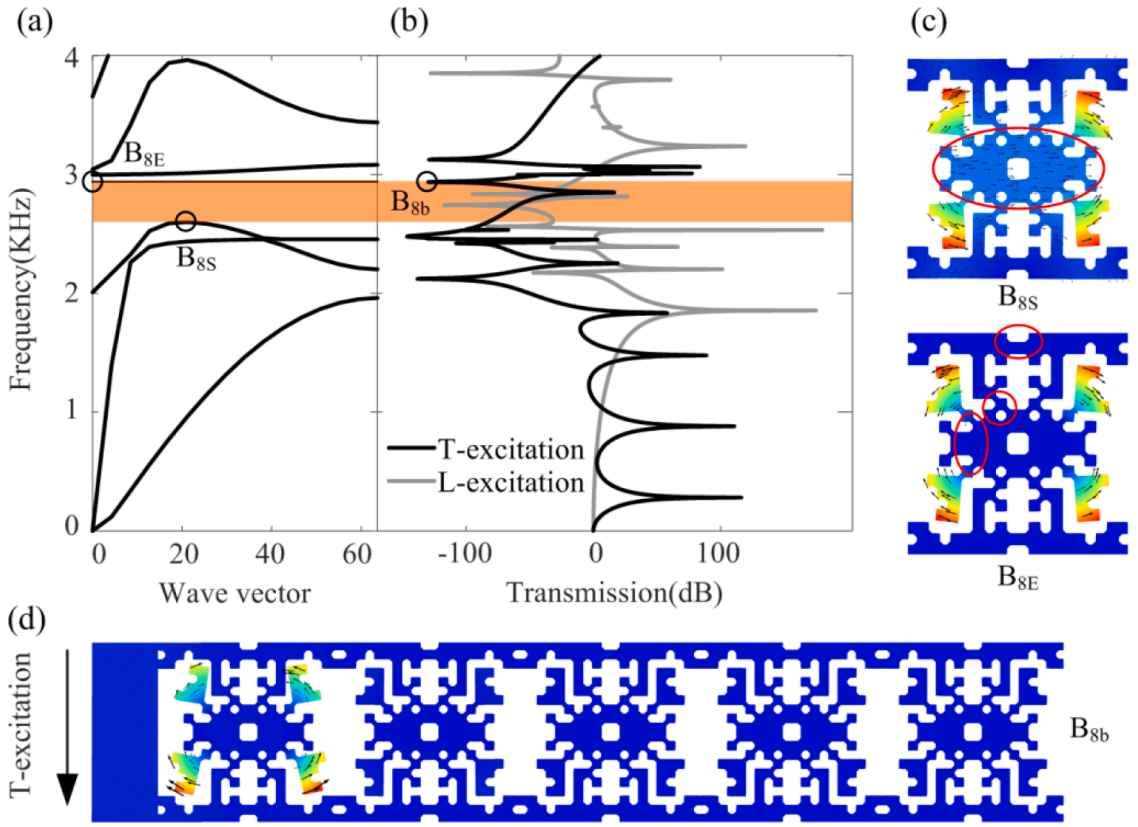

Fig. 16. (color online) Relevant calculation results of the substructure B_8 in the population of the 80th generation under bisymmetry constraints. (a) The band structure, (b) the transfer function curves of corresponding cantilever beam under transverse excitation (T-excitation) and longitudinal excitation (L-excitation), (c) the eigenmodes B_{8S} and B_{8E} labeled in the band structure, and (d) cantilever vibration mode B_{8b} under T-excitation inside the band gap frequency range.

disconnection of the topology at some key positions have an important impact on the vibration isolation characteristics and support characteristics of the obtained individual.

4.3. Numerical results under longitudinal and transverse bisymmetry constraints

The topology optimization under longitudinal and transverse bisymmetry constraints inside substructures is also analyzed. Fig. 14 shows the distribution of objective functions values T_1 and T_2 of individuals of the population corresponding to some evolutionary generations. It can be seen from Fig. 14 that the distribution of objective function values of the initial population ($G = 1$) individuals has good diversity. As the evolutionary generation increases, the two objective functions values gradually converge to the local Pareto front. The six representative individual substructures ranking No. B_1, B_2, B_3, B_7, B_8 and B_{17} under the maximum evolutionary generation ($G = 80$) are singled out from the local Pareto front as shown in Fig. 14(b). Table 3 presents more comprehensive calculation results corresponding to these six substructures.

It can be seen from Fig. 14(b) that under the bisymmetry constraints, the six individuals in the final evolutionary population have certain similarities in configuration. All substructures have strong continuous structures at the upper and lower boundaries in the width direction of the cantilever beam to maintain the overall support stiffness, and the local structures located between the above continuous boundaries contribute to the generation of vibration bandgaps. Among them, in the local structure of individuals ranking No. B_1, B_3 and B_8, there are four symmetrically distributed cantilever mass blocks, which are easy to produce local resonance under external excitation. Closed areas with pores can be found in the substructure corresponding to the individuals ranking No. B_2, B_7 and B_{17}. These closed areas are connected with the front and rear substructures only through the upper and lower continuous boundaries. Compared with the individuals ranking No. B_1, B_3 and B_8, the local thin beams connecting their upper and lower boundaries have a larger span in the length direction of the cantilever beam, and there are no large mass blocks supported by the soft cantilevers in the closed areas. These internal structural features increase the stiffness of the substructures with closed areas and make it less prone to local resonance.

It can be seen from the data listed in Table 3 that the T_1 increases in order of substructure B_1, B_3, B_8, B_{17}, B_7, B_2, the w_{gp1} is basically compounded this law. While T_2 decreases in the above order, and the f_{mod1} is basically compounded the same law. The distribution laws of the start frequency f_{gs1}, the end frequency f_{ge1} and the center frequency f_{gc1} of the bandgap are not so obvious.

It can be inferred from the extremely narrow band gap width (only 33 Hz) and significant internal cantilever large mass blocks of substructure B_1 that the band gap of substructureB_1 belongs to local resonance type. On the contrary, from the extremely wide band gap (up to 17,704 Hz) of substructure B_2 and no obvious cantilever mass inside, it can be inferred that its band gap belongs to Bragg scattering type. The band gap characteristics of the remaining substructures B_3, B_8, B_{17} and B_7 will be further analyzed in combination with other information.

Relevant calculation results of the substructures B_3, B_8, B_{17} and B_7 are showed in Figs. 15–18 for in-depth analysis.

The first band gap of substructure B_3 starts from the maximum point B_{3S} on the 3rd band, and a flat band falls into it, as shown in Fig. 15(a). As can be seen from Fig. 15(b), when one end of the cantilever composed of substructure B_3 is transversely excited, the response amplitude of the free end of the cantilever relative to the input end is significantly reduced within the band gap frequency range, which proves the

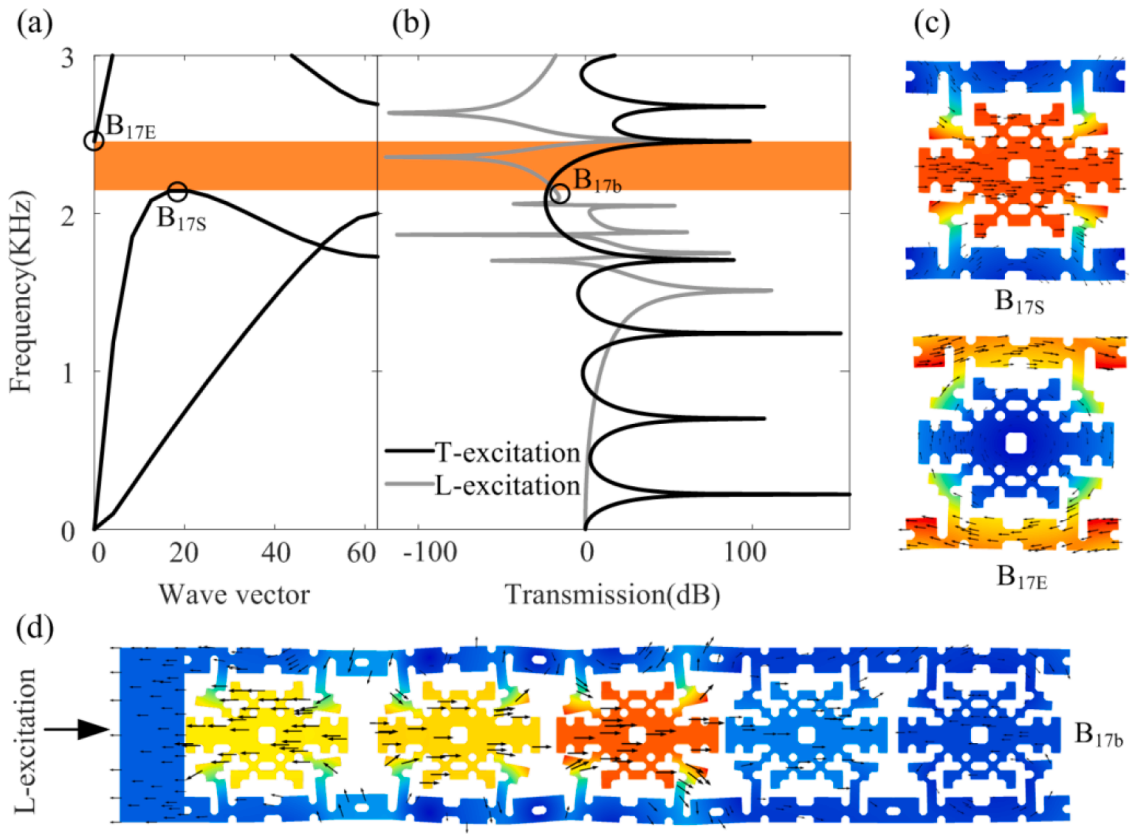

Fig. 17. (color online) Relevant calculation results of the substructure B_{17} in the population of the 80th generation under bisymmetry constraints. (a) The band structure, (b) the transfer function curves of corresponding cantilever beam under transverse excitation (T-excitation) and longitudinal excitation (L-excitation), (c) the eigenmodes B_{17S} and B_{17E} labeled in the band structure, and (d) cantilever vibration mode B_{17b} under L-excitation inside the band gap frequency range.

existence of the band gap and the vibration suppression effect of the band gap. According to the substructure modal shapes corresponding to the band gap start frequency and end frequency shown in Fig. 15(c) and the vibration mode of the cantilever beam corresponding to B_{3b} point on the transverse excitation transfer function curve shown in Fig. 15(d), the main vibration energy is localized in the swing movement of four symmetrically distributed cantilever mass blocks, and the vibration propagation on the simplest continuous path of the front and rear substructures is weakened. The remaining part between the upper and lower continuous boundaries does not participate in the local resonance of the cantilever mass, but its existence helps to improve the overall structural stiffness of the cantilever beam. Further, combined with the narrow width and lower start frequency, it can be judged that the first band gap of substructure B_3 is a local resonance band gap.

The first band gap of substructure B_8 starts from the maximum point B_{8S} on the 3rd band, and a flat band falls into it, as shown in Fig. 16(a). When the cantilever beam composed of substructure B_8 is subjected to transverse excitation and longitudinal excitation respectively, it both shows a significant decrease in the response amplitude of the vibration transfer curve in the whole first band gap frequency range, as shown in Fig. 16(b). From the substructure vibration mode B_{8S} corresponding to the band gap starting frequency, it can be found that in addition to the swing motion of the four cantilever masses, the central mass part where the four cantilever masses are located (the circular region in the B_{8S} subgraph) shows a transverse motion. This B_{8S} mode reflects the characteristics of the start frequency mode of both the local resonance gaps and Bragg scattering gaps at the same time. The end frequency mode B_{8E} of the band gap and the vibration mode B_{8b} of the cantilever beam have the similar vibration shape with those of substructure B_3. It can be seen from Table 3 that the band gap width of substructure B_8 is 335 Hz, which is about three times that of B_3(112 Hz). The fundamental frequency (277 Hz) of B_8 cantilever beam is slightly higher than that of B_3 cantilever beam (252 Hz), but the band gap starting frequency of B_8 increases significantly (2571 Hz for B_8 and 2178 Hz for B_3). It can be seen from the data comparison that substructure B_8 is stronger than substructure B_3. The difference of the topological structures can explain the difference of these data. As shown in the B_{8E} subgraph of Fig. 16(c), the circled three positions of substructure B_8 are stronger than those of substructure B_3. Among them, the increase of real meshes between the upper and lower cantilever mass blocks shortens the local cantilever length of the mass block and improves the starting frequency of local resonance, that is, the starting frequency of band gap. The increase of real meshes at the other two circled positions improves the overall structural height of the cantilever beam, so as to improve the fundamental frequency of the cantilever beam.

The first band gap of substructure B_{17} appears between the 2nd band and the 3rd band, and there is no flat band near the band gap, as shown in Fig. 17(a). Fig. 17(b) shows that when the cantilever beam composed of substructure B_{17} is longitudinally excited, there is obvious attenuation of the response amplitude in the band gap frequency range. The vibration energy of the mode B_{17S} corresponding to the start frequency of the band gap is concentrated in the transverse motion of the internal structure located between the upper and lower continuous boundaries. The main vibration energy of mode B_{17E} corresponding to the band gap termination frequency is on the upper and lower continuous boundaries, and the rest part between the boundaries also participates in the vibration to a small extent. On the whole, it looks just like the relative movement of panzer chains (the upper and lower continuous boundary) and a tank wheel (the rest part between the boundaries). From Fig. 17 (d), it can be seen that the vibration energy attenuates from the input end to the output end of the cantilever beam. From the distribution of the vibration energy of the mode of the band gap start frequency and the

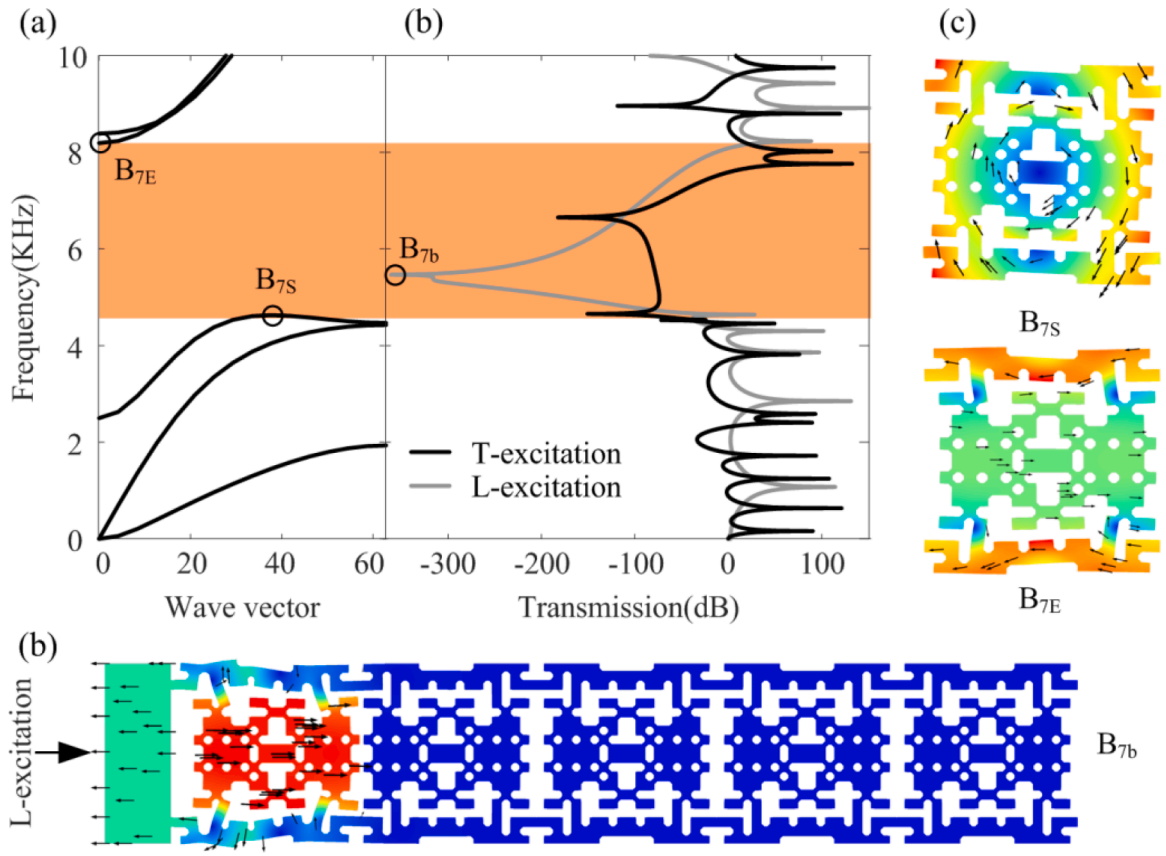

Fig. 18. (color online) Relevant calculation results of the substructure B_7 in the population of the 80th generation under bisymmetry constraints. (a) The band structure, (b) the transfer function curves of corresponding cantilever beam under transverse excitation (T-excitation) and longitudinal excitation (L-excitation), (c) the eigenmodes B_{7S} and B_{7E} labeled in the band structure, and (d) cantilever vibration mode B_{7b} under L-excitation inside the band gap frequency range.

vibration mode of the cantilever beam, there is no obvious local resonance phenomenon. Therefore, the band gap of substructure B_{17} reflects the characteristics of Bragg scattering band gap as a whole.

The first band gap of substructure B_7 starts from the point B_{7S} (4565 Hz) on the 3rd band and ends at the point B_{7E} (8075 Hz) on the 4th band, as shown in Fig. 18(a). Compared with substructures B_8 and B_{17}, substructure B_7 has a much higher and wider band gap. The response transfer curves of the cantilever beam composed of substructure B_7 under longitudinal excitation and transverse excitation both show very significant attenuation in the band gap frequency range. As shown in Fig. 18(b), the maximum attenuation amplitude can reach more than 300 dB. Fig. 18(c) shows that the band gap start mode B_{7S} and end mode B_{7E} do not have local resonance, but the vibration mode in which all real meshes of the substructure participate together. From the vibration mode corresponding to the frequency point B_{7b} when the cantilever beam composed of substructure B_7 is longitudinally excited, the vibration energy decays rapidly after passing through the first substructure, as shown in Fig. 18(d). Based on the above analysis, it can be concluded that the first band gap of substructure B_7 is a typical Bragg scattering band gap.

Based on the above analysis of the numerical simulation results under longitudinal and transverse bisymmetry constraints, a similar analysis conclusion with transverse symmetric constraints can be drawn. In other words, the smaller the T_1 value, the better the overall support stiffness of the corresponding structure, accompanied by a lower and narrower local resonance band gap. On the contrary, the smaller the T_2 value, the worse the overall support stiffness of the corresponding structure, accompanied by a higher and wider Bragg scattering band gap. The interaction of local resonance and Bragg scattering can be found in the vibration mode corresponding to the band gap start frequency of substructure B_8 with compromise T_1 and T_2. In addition, it can be seen from the vibration transfer curves of the cantilever beams that the vibration attenuation in the band gap frequency range of the individual with better T_2 value are more significant than that of the individual with better T_1 value. One difference is that the first local resonant band gap of individuals with bisymmetry constraints, such as substructure B_3 and B_8, starts from the 3rd band and is accompanied by a flat band near the end of the band gap. While the first local resonant band gap of individuals with transverse symmetry constraints, such as substructure S_3 and S_9, starts from the 2nd band, and there is no flat band near the end of the band gap. Comparing the data in Tables 2 and 3, we can draw a conclusion similar to that in many literatures, that is, reducing the symmetry constraint in the topology optimization of PnCs helps to obtain a lower and wider band gap.

5. Conclusions

Taking a two-dimensional cantilever beam as an example, this paper attempts to realize the integrated design of vibration isolation and support of macro structure through the multi-objective topology optimization design of periodic substructures. The structural vibration isolation is based on the elastic wave band gap characteristics of periodic structures. Two dimensionless objective functions T_1 and T_2 are set to ensure that the obtained topology results have sufficient overall structural stiffness as well as low and wide band gap. Based on GA and FEM, a set of calculation flow is established to realize the search iteration of available substructures and the solution of the corresponding objective functions.

Based on the traditional NSGA-II, an improved multi-objective GA is proposed to improve the convergence speed and avoid invalid operation

and repeated operation. It is proposed to identify valid individuals through maze path-finding, eliminate invalid island real meshes, and prohibit duplicate individuals in the population to maintain population diversity and avoid repeated calculation. The effectiveness of the relevant improvement measures is verified by a simple example compared with the traditional NSGA-II. While Mesh generation strategy combining coarse mesh and fine mesh are used to reduce the scale of GA search space and ensure the accuracy of finite element solution.

Using the proposed algorithm, the multi-objective topology optimization of the periodic substructure constituting the cantilever beam is carried out with transverse symmetry constraints and transverse plus longitudinal bisymmetry constraints, respectively. Representative individuals are selected from the Pareto front of T_1 and T_2 of the last generation for in-depth analysis. The numerical results show that under the same operation parameters and model parameters, the substructures with lower symmetry constraints is easier to obtain lower and wider band gap. Individuals close to the optimal value of T_1 are more likely to obtain higher overall structural stiffness and lower and narrower local resonance band gap. On the contrary, individuals close to the optimal value of T_2 have wider and higher Bragg scattering band gap and weaker overall structural stiffness, and the vibration attenuation amplitude of corresponding cantilever beams in the band gap frequency range is more significant. The structural characteristics of some key positions in the substructures, such as the length of the local cantilever beams, the size of the cantilever mass blocks, the span between the thin beams of the closed areas, etc., have an important impact on the location and the width of the band gap, as well as the fundamental frequency of the overall cantilever beam. In a substructure with compromise values of T_1 and T_2, the vibration mode corresponding to the start frequencies of local resonance band gap and Bragg scattering band gap are observed at the same time.

The numerical results show that the proposed algorithm is effective for the integrated structural design of support and vibration isolation. But the optimized shape obtained from the simulation results is complex. This is mainly caused by using coarser meshes in order to improve the convergence speed and reduce the amount of computation. The small number of initial meshes leads to rough 'polyline' topological geometric boundaries. Although the topology structures shown in this paper can be manufactured by 3D printing or the wire EDM (Electrical Discharge Machining) method or a water jet cutter, the cost and difficulty are relatively high. In order to solve this problem, at least two schemes can be adopted in the follow-up research work. One is to increase the number of meshes at the cost of increasing the amount of computation and slowing down the convergence speed, so as to make the obtained structural topology contour more rounded. Second, based on the current topology optimization results, further shape optimization and adjustment are carried out to make it easier to process and manufacture.

CRediT authorship contribution statement

Haojiang Zhao: Conceptualization, Methodology, Writing – review & editing. **Yang Feng:** Software, Validation, Data curation, Writing – original draft. **Wei Li:** Supervision, Investigation. **Chuang Xue:** Formal analysis, Resources, Project administration.

Declaration of Competing Interest

On behalf of all authors, the corresponding author states that there is no conflict of interest.

Data Availability

The authors do not have permission to share data.

Acknowledgment

This work is supported by the National Natural Science Foundation of China (Grant No. 51805510).

References

[1] Maute K, Sigmund O. Topology optimization approaches: a comparative review. Struct Multidiscip Optim 2013;48(6):1031–55. https://doi.org/10.1007/s00158-013-0978-6.
[2] Van Dijk NP, Maute K, Langelaar M, Van Keulen F. Level-set methods for structural topology optimization: a review. Struct Multidiscip Optim 2013;48(3):437–72. https://doi.org/10.1007/s00158-013-0912-y.
[3] Huang X, Xie YM. A further review of ESO type methods for topology optimization. Struct Multidiscip Optim 2010;41(5):671–83. https://doi.org/10.1007/s00158-010-0487-9.
[4] Yu D, Liu Y, Wang G, Zhao H, Qiu J. Flexural vibration band gaps in Timoshenko beams with locally resonant structures. J Appl Phys 2006;100(12):124901. https://doi.org/10.1063/1.2400803.
[5] Sigalas MM, Economou EN. Elastic and acoustic wave band structure. J Sound Vib 1992;158(2):377–82. https://doi.org/10.1016/0022-460X(92)90059-7.
[6] Kushwaha MS, Halevi P, Dobrzynski L, Djafari-Rouhani B. Acoustic band structure of periodic elastic composites. Phys Rev Lett 1993;71(13):2022–5. https://doi.org/10.1103/PhysRevLett.71.2022.
[7] Martínez-Sala R, Sancho J, Sánchez JV, Gómez V, Llinares J, Meseguer F. Sound attenuation by sculpture. Nature 1995;378(6554):241. https://doi.org/10.1038/378241a0. 241.
[8] Liu Z, Zhang X, Mao Y, Zhu YY, Yang Z, Chan CT, Sheng P. Locally resonant sonic materials. Science 2000;289(5485):1734–6. https://doi.org/10.1126/science.289.5485.1734.
[9] Vasseur JO, Deymier PA, Chenni B, Djafari-Rouhani B, Dobrzynski L, Prevost D. Experimental and theoretical evidence for the existence of absolute acoustic band gaps in two-dimensional solid phononic crystals. Phys Rev Lett 2001;86(14):3012. https://doi.org/10.1103/PhysRevLett.86.3012.
[10] Claeys CC, Vergote K, Sas P, Desmet W. On the potential of tuned resonators to obtain low-frequency vibrational stop bands in periodic panels. J Sound Vib 2013;332(6):1418–36. https://doi.org/10.1016/j.jsv.2012.09.047.
[11] Matlack KH, Bauhofer A, Krödel S, Palermo A, Daraio C. Composite 3D-printed metastructures for low-frequency and broadband vibration absorption. Proc Natl Acad Sci USA 2016;13(30):8386–90. https://doi.org/10.1073/pnas.1600171113.
[12] Gao P, Climente A, Sánchez-Dehesa J, Wu L. Single-phase metamaterial plates for broadband vibration suppression at low frequencies. J Sound Vib 2019;444:108–26. https://doi.org/10.1016/j.jsv.2018.12.022.
[13] Yao Z, Zega V, Su Y, Zhou Y, Ren J, Zhang J, Corigliano A. Design, fabrication and experimental validation of a metaplate for vibration isolation in MEMS. J Microelectromech Syst 2020;29(5):1401–10. https://doi.org/10.1109/JMEMS.2020.3016179.
[14] Liu P, Zuo S, Wu X, Sun L, Zhang Q. Study on the vibration attenuation property of one finite and hybrid piezoelectric phononic crystal beam. Eur J Mech A Solids 2020;84:104017. https://doi.org/10.1016/j.euromechsol.2020.104017.
[15] Guo JC, Li JR, Zhang Z. Interface design of low-frequency band gap characteristics in stepped hybrid phononic crystals. Appl Acoust 2021;182:108209. https://doi.org/10.1016/j.apacoust.2021.108209.
[16] Xu X, Barnhart MV, Li X, Chen Y, Huang G. Tailoring vibration suppression bands with hierarchical metamaterials containing local resonators. J Sound Vib 2019;442:237–48. https://doi.org/10.1016/j.jsv.2018.10.065.
[17] Krushynska AO, Amendola A, Bosia F, Daraio C, Pugno NM, Fraternali F. Accordion-like metamaterials with tunable ultra-wide low-frequency band gaps. New J Phys 2018;20(7):073051. https://doi.org/10.1088/1367-2630/aad354.
[18] Choi MJ, Oh MH, Koo B, Cho S. Optimal design of lattice structures for controllable extremal band gaps. Sci Rep 2019;9(1):1–13. https://doi.org/10.1038/s41598-019-46089-9.
[19] Muhammad, Lim CW, Li JTH, Zhao Z. Lightweight architected lattice phononic crystals with broadband and multiband vibration mitigation characteristics. Extrem Mech Lett 2020;41:100994. https://doi.org/10.1016/j.eml.2020.100994.
[20] Dal Poggetto VF, Bosia F, Miniaci M, Pugno NM. Optimization of spider web-inspired phononic crystals to achieve tailored dispersion for diverse objectives. Mater Des 2021;209:109980. https://doi.org/10.1016/j.matdes.2021.109980.
[21] Chen YY, Hu GK, Huang GL. An adaptive metamaterial beam with hybrid shunting circuits for extremely broadband control of flexural waves. Smart Mater Struct 2016;25(10):105036. https://doi.org/10.1088/0964-1726/25/10/105036.
[22] Liang F, Chen Y, Gong JJ, Qian Y. Vibration self-suppression of spinning fluid-conveying pipes composed of periodic composites. Int J Mech Sci 2022;220:107150. https://doi.org/10.1016/j.ijmecsci.2022.107150.
[23] Hedayatrasa S, Kersemans M, Abhary K, Van Paepegem W. Introducing obliquely perforated phononic plates for enhanced bandgap efficiency. Materials 2018;11(8):1309. https://doi.org/10.3390/ma11081309 (Basel).
[24] Barnhart MV, Xu X, Chen Y, Zhang S, Song J, Huang G. Experimental demonstration of a dissipative multi-resonator metamaterial for broadband elastic wave attenuation. J Sound Vib 2019;438:1–12. https://doi.org/10.1016/j.jsv.2018.08.035.
[25] Yang Q, Song T, Wen XD, Zhu HF, Tan ZH, Liu LJ, Liu ZJ, Sun XW. Simulations on the wide bandgap characteristics of a two-dimensional tapered scatterer phononic

crystal slab at low frequency. Phys Lett A 2020;384(35):126885. https://doi.org/10.1016/j.physleta.2020.126885.
[26] Zhao P, Zhang K, Zhao C, Qi L, Deng Z. In-plane wave propagation analysis for waveguide design of hexagonal lattice with Koch snowflake. Int J Mech Sci 2021;209:106724. https://doi.org/10.1016/j.ijmecsci.2021.106724.
[27] Panahi E, Hosseinkhani A, Khansanami MF, Davood Younesian D, Ranjbar M. Novel cross shape phononic crystals with broadband vibration wave attenuation characteristic: design, modeling and testing. Thin Wall Struct 2021;163:107665. https://doi.org/10.1016/j.tws.2021.107665.
[28] Leroy V, Bretagne A, Fink M, Willaime H, Tabeling P, Tourin A. Design and characterization of bubble phononic crystals. Appl Phys Lett 2009;95(17):171904. https://doi.org/10.1063/1.3254243.
[29] Elmadih W, Chronopoulos D, Syam WP, Maskery I, Meng H, Leach RK. Three-dimensional resonating metamaterials for low-frequency vibration attenuation. Sci Rep 2019;9(1):1–8. https://doi.org/10.1038/s41598-019-47644-0.
[30] Lu X, Wu X, Xiang H, Shen J, Li Y, Li Y, Wang X. Triple tunability of phononic bandgaps for three-dimensional printed hollow sphere lattice metamaterials. Int J Mech Sci 2022;221:107166. https://doi.org/10.1016/j.ijmecsci.2022.107166.
[31] Zhu X, Zhong S, Zhao H. Band gap structures for viscoelastic phononic crystals based on numerical and experimental investigation. Appl Acoust 2016;106:93–104. https://doi.org/10.1016/j.apacoust.2016.01.007.
[32] Li FL, Zhang C, Wang YS. Analysis of the effects of viscosity on the SH-wave band-gaps of 2D viscoelastic phononic crystals by Dirichlet-to-Neumann map method. Int J Mech Sci 2021;195:106225. https://doi.org/10.1016/j.ijmecsci.2020.106225.
[33] Chen Y, Li T, Scarpa F, Wang L. Lattice metamaterials with mechanically tunable Poisson's ratio for vibration control. Phys Rev Appl 2017;7(2):024012. https://doi.org/10.1103/PhysRevApplied.7.024012.
[34] Huang Y, Li J, Chen W, Bao R. Tunable bandgaps in soft phononic plates with spring-mass-like resonators. Int J Mech Sci 2019;151:300–13. https://doi.org/10.1016/j.ijmecsci.2018.11.029.
[35] Hedayatrasa S, Abhary K, Uddin MS, Guest JK. Optimal design of tunable phononic bandgap plates under equibiaxial stretch. Smart Mater Struct 2016;25(5):055025. https://doi.org/10.1088/0964-1726/25/5/055025.
[36] Yi G, Youn BD. A comprehensive survey on topology optimization of phononic crystals. Struct Multidiscip Optim 2016;54(5):1315–44. https://doi.org/10.1007/s00158-016-1520-4.
[37] Li W, Meng F, Chen Y, Li YF, Huang X. Topology optimization of photonic and phononic crystals and metamaterials: a review. Adv Theory Simul 2019;2(7):1900017. https://doi.org/10.1002/adts.201900017.
[38] Ma M, Wang L. Reliability-based topology optimization framework of two-dimensional phononic crystal band-gap structures based on interval series expansion and mapping conversion method. Int J Mech Sci 2021;196:106265. https://doi.org/10.1016/j.ijmecsci.2020.106265.
[39] Li Y, Huang X, Meng F, Zhou S. Evolutionary topological design for phononic band gap crystals. Struct Multidiscip Optim 2016;54(3):595–617. https://doi.org/10.1007/s00158-016-1424-3.
[40] Zhang Z, Li YF, Meng F, Huang X. Topological design of phononic band gap crystals with sixfold symmetric hexagonal lattice. Comput Mater Sci 2017;139:97–105. https://doi.org/10.1016/j.commatsci.2017.07.037.
[41] Chen Y, Huang X, Sun G, Yan X, Li G. Maximizing spatial decay of evanescent waves in phononic crystals by topology optimization. Comput Struct 2017;182:430–47. https://doi.org/10.1016/j.compstruc.2017.01.001.
[42] Wang K, Liu Y, Wang B. Follow-up optimized phononic band structure design based on reserved inclusions. Phys B 2019;564:157–65. https://doi.org/10.1016/j.physb.2019.04.001.
[43] Wang K, Liu Y, Wang B. Ultrawide band gap design of phononic crystals based on topological optimization. Phys B 2019;571:263–72. https://doi.org/10.1016/j.physb.2019.07.012.
[44] Huang Y, Liu S, Zhao J. A gradient-based optimization method for the design of layered phononic band-gap materials. Acta Mech Solida Sin 2016;29(4):429–43. https://doi.org/10.1016/S0894-9166(16)30245-2.
[45] Liu W, Yoon GH, Yi B, Choi H, Yang Y. Controlling wave propagation in one-dimensional structures through topology optimization. Comput Struct 2020;241:106368. https://doi.org/10.1016/j.compstruc.2020.106368.
[46] Zhang Z, Ji GM, Han XK. Optimization design of a novel zigzag lattice phononic crystal with holes. Int J Mod Phys B 2019;33(13):1950124. https://doi.org/10.1142/S0217979219501248.
[47] Wang SY, Tai K. Structural topology design optimization using genetic algorithms with a bit-array representation. Comput Methods Appl Mech Eng 2005;194(36–38):3749–70. https://doi.org/10.1016/j.cma.2004.09.003.
[48] Hussein MI, Hamza K, Hulbert GM, Saitou K. Optimal synthesis of 2D phononic crystals for broadband frequency isolation. Wave Random Complex 2007;17(4):491–510. https://doi.org/10.1080/17455030701501869.
[49] Gazonas GA, Weile DS, Wildman R, Mohan A. Genetic algorithm optimization of phononic bandgap structures. Int J Solids Struct 2006;43(18–19):5851–66. https://doi.org/10.1016/j.ijsolstr.2005.12.002.
[50] Liu ZF, Wu B, He CF. Band-gap optimization of two-dimensional phononic crystals based on genetic algorithm and FPWE. Wave Random Complex 2014;24(3):286–305. https://doi.org/10.1080/17455030.2014.901582.
[51] Xie L, Xia B, Liu J, Huang G, Lei J. An improved fast plane wave expansion method for topology optimization of phononic crystals. Int J Mech Sci 2017;120:171–81. https://doi.org/10.1016/j.ijmecsci.2016.11.023.
[52] Han XK, Zhang Z. Topological optimization of phononic crystal thin plate by a genetic algorithm. Sci Rep 2019;9(1):1–13. https://doi.org/10.1038/s41598-019-44850-8.
[53] Han XK, Zhang Z. Bandgap design of three-phase phononic crystal by topological optimization. Wave Motion 2020;93:102496. https://doi.org/10.1016/j.wavemoti.2019.102496.
[54] Dong HW, Su XX, Wang YS. Multi-objective optimization of two-dimensional porous phononic crystals. J Phys D Appl Phys 2014;47(15):155301. https://doi.org/10.1088/0022-3727/47/15/155301.
[55] Hussein MI, Hamza K, Hulbert GM, Scott RA, Saitou K. Multiobjective evolutionary optimization of periodic layered materials for desired wave dispersion characteristics. Struct Multidiscip Optim 2006;31(1):60–75. https://doi.org/10.1007/s00158-005-0555-8.
[56] Dong HW, Su XX, Wang YS, Zhang C. Topology optimization of two-dimensional asymmetrical phononic crystals. Phys Lett A 2014;378(4):434–41. https://doi.org/10.1016/j.physleta.2013.12.003.
[57] Romero-García V, Sánchez-Pérez JV, García-Raffi LM, Herrero JM, García-Nieto S, Blasco X. Hole distribution in phononic crystals: design and optimization. J Acoust Soc Am 2009;125(6):3774–83. https://doi.org/10.1121/1.3126948.
[58] Dong HW, Wang YS, Wang YF, Zhang C. Reducing symmetry in topology optimization of two-dimensional porous phononic crystals. AIP Adv 2015;5(11):117149. https://doi.org/10.1063/1.4936640.
[59] Dong HW, Wang YS, Zhang C. Topology optimization of chiral phoxonic crystals with simultaneously large phononic and photonic bandgaps. IEEE Photonics J 2017;9(2):1–16. https://doi.org/10.1109/JPHOT.2017.2665700.
[60] Xu W, Ning J, Zhang M, Wang W, Yang T. Three-phase microstructure topology optimization of two-dimensional phononic bandgap materials using genetic algorithms. Acta Mech Solida Sin 2018;31(6):775–84. https://doi.org/10.1007/s10338-018-0036-4.
[61] Sigmund O, Søndergaard Jensen J. Systematic design of phononic band–gap materials and structures by topology optimization. Philos Trans R Soc A 2003;361(1806):1001–19. https://doi.org/10.1098/rsta.2003.1177.
[62] Zhang X, He J, Takezawa A, Kang Z. Robust topology optimization of phononic crystals with random field uncertainty. Int J Numer Methods Eng 2018;115(9):1154–73. https://doi.org/10.1002/nme.5839.
[63] Li X, Ning S, Liu Z, Yan Z, Luo C, Zhuang Z. Designing phononic crystal with anticipated band gap through a deep learning based data-driven method. Comput Methods Appl Mech Eng 2020;361:112737. https://doi.org/10.1016/j.cma.2019.112737.
[64] Deb K, Pratap A, Agarwal S, Meyarivan T. A fast and elitist multiobjective genetic algorithm: NSGA-II. IEEE Trans Evol Comput 2002;6(2):182–97. https://doi.org/10.1109/4235.996017.
[65] Hedayatrasa S, Abhary K, Uddin M. Numerical study and topology optimization of 1D periodic bimaterial phononic crystal plates for bandgaps of low order Lamb waves. Ultrasonics 2015;57:104–24. https://doi.org/10.1016/j.ultras.2014.11.001.
[66] Dong HW, Su XX, Wang YS, Zhang C. Topological optimization of two-dimensional phononic crystals based on the finite element method and genetic algorithm. Struct Multidiscip Optim 2014;50(4):593–604. https://doi.org/10.1007/s00158-014-1070-6.
[67] Zhu R, Liu XN, Hu GK, Sun CT, Huang GL. A chiral elastic metamaterial beam for broadband vibration suppression. J Sound Vib 2014;333(10):2759–73. https://doi.org/10.1016/j.jsv.2014.01.009.
[68] Chen YY, Barnhart MV, Chen JK, Hu GK, Sun CT, Huang GL. Dissipative elastic metamaterials for broadband wave mitigation at subwave length scale. Compos Struct 2016;136:358–71. https://doi.org/10.1016/j.compstruct.2015.09.048.
[69] Xie L, Xia B, Huang G, Lei J, Liu J. Topology optimization of phononic crystals with uncertainties. Struct Multidiscip Optim 2017;56(6):1319–39. https://doi.org/10.1007/s00158-017-1723-3.
[70] Zhang X, Takezawa A, Kang Z. A phase-field based robust topology optimization method for phononic crystals design considering uncertain diffuse regions. Comput Mater Sci 2019;160:159–72. https://doi.org/10.1016/j.commatsci.2018.12.057.
[71] Chen Y, Meng F, Sun G, Li G, Huang X. Topological design of phononic crystals for unidirectional acoustic transmission. J Sound Vib 2017;410:103–23. https://doi.org/10.1016/j.jsv.2017.08.015.
[72] Li S, Dou Y, Chen T, Wan Z, Ju L, Zhang F, Cui XX. Forming low-frequency complete vibration bandgaps in a thin nonmetallic elastic metamaterial plate. Acoust Phys 2019;65(3):322–33. https://doi.org/10.1134/S1063771019030084.
[73] Cheng Q, Guo H, Yuan T, Sun P, Guo F, Wang Y. Topological design of square lattice structure for broad and multiple band gaps in low-frequency range. Extrem Mech Lett 2020;35:100632. https://doi.org/10.1016/j.eml.2020.100632.
[74] Zhang Z, Han XK. A new hybrid phononic crystal in low frequencies. Phys Lett A 2016;380(45):3766–72. https://doi.org/10.1016/j.physleta.2016.09.019.
[75] Guo JC, Li JR, Zhang L, Zhang Z. Wide range of wave attenuation in beam-supported stepped hybrid phononic crystals. Wave Motion 2022;108:102827. https://doi.org/10.1016/j.wavemoti.2021.102827.
[76] Goto AM, Nobrega ED, Pereira FN, Dos Santos JMC. Numerical and experimental investigation of phononic crystals via wave-based higher-order rod models. Int J Mech Sci 2020;181:105776. https://doi.org/10.1016/j.ijmecsci.2020.105776.
[77] Yang XW, Lee JS, Kim YY. Effective mass density based topology optimization of locally resonant acoustic metamaterials for bandgap maximization. J Sound Vib 2016;383:89–107. https://doi.org/10.1016/j.jsv.2016.07.022.
[78] Yuksel O, Yilmaz C. Realization of an ultrawide stop band in a 2-D elastic metamaterial with topologically optimized inertial amplification mechanisms. Int J Solids Struct 2020;203:138–50. https://doi.org/10.1016/j.ijsolstr.2020.07.018.
[79] Chen Y, Guo D, Li YF, Li G, Huang X. Maximizing wave attenuation in viscoelastic phononic crystals by topology optimization. Ultrasonics 2019;94:419–29. https://doi.org/10.1016/j.ultras.2018.05.005.

[80] Chen Y, Wang L. Harnessing structural hierarchy to design stiff and lightweight phononic crystals. Extrem Mech Lett 2016;9:91–6. https://doi.org/10.1016/j.eml.2016.05.009.
[81] Andreassen E, Jensen JS. Topology optimization of periodic microstructures for enhanced dynamic properties of viscoelastic composite materials. Struct Multidiscip Optim 2014;49(5):695–705. https://doi.org/10.1007/s00158-013-1018-2.
[82] Dong HW, Wang YS, Ma TX, Su XX. Topology optimization of simultaneous photonic and phononic bandgaps and highly effective phoxonic cavity. J Opt Soc Am B 2014;31(12):2946–55. https://doi.org/10.1364/JOSAB.31.002946.
[83] Hedayatrasa S, Kersemans M, Abhary K, Uddin M, Van Paepegem W. Optimization and experimental validation of stiff porous phononic plates for widest complete bandgap of mixed fundamental guided wave modes. Mech Syst Signal Process 2018;98:786–801. https://doi.org/10.1016/j.ymssp.2017.05.019.
[84] Hedayatrasa S, Abhary K, Uddin M, Ng CT. Optimum design of phononic crystal perforated plate structures for widest bandgap of fundamental guided wave modes and maximized in-plane stiffness. J Mech Phys Solids 2016;89:31–58. https://doi.org/10.1016/j.jmps.2016.01.010.
[85] Cheung SK, Chan TL, Zhang ZQ, Chan CT. Large photonic band gaps in certain periodic and quasiperiodic networks in two and three dimensions. Phys Rev B 2004;70(12):125104. https://doi.org/10.1103/PhysRevB.70.125104.